Blind-time domain motion compensation of and significant-wave height extraction from high-frequency (HF) radar data acquired on a floating platform

by

© **Seyedehsepideh Hashemi**

Department of Electrical and Computer Engineering

Memorial University

May 2023

St. John's, Newfoundland and Labrador, Canada

Abstract

High-frequency surface wave radar (HFSWR) is recognized as one of the essential tools for remote sensing of the ocean surface. It provides wide-area, all-weather, and near-real time surveillance. However, extracting useful information when the radar is mounted on a floating platform can be challenging since the platform motion may considerably affect and contaminate the high-frequency (HF) radar Doppler spectrum. The usual procedure for extracting ocean surface information from a high-frequency surface wave radar transmitting from a floating platform is to first compensate for the motion of the antenna in the acquired motion-contaminated Doppler spectrum and then extract the ocean wave parameters from the motion-compensated result.

Two methods for motion compensation of HF radar signals for the case of a floating transmitter and fixed receiver are proposed when the motion parameters (including the amplitude and angular frequency of the motion) are not known *a priori*. This study assumes that the floating platform follows a single-frequency motion model. In the first method which is a time-domain technique, we estimate motion parameters from the autocorrelation function of the received electric field. The autocorrelation is related to the received radar cross section by application of an inverse temporal Fourier transform. The motion parameters are estimated by comparing the locations of the zeros of the autocorrelation function for the fixed antenna case with those for an antenna on a floating platform. Then, the zeros associated with the platform motion can be found.

Alternatively, in the second method which is a frequency-domain approach, we aimed to estimate platform-motion parameters from the received motion-contaminated Doppler spectrum, which is proportional to the observed radar cross-section of the ocean surface from the floating platform. Motion parameters are determined from

the relation between the locations and amplitudes of the Bragg peaks and motion-induced peaks, and the amplitude and angular frequency of the motion, respectively. While the results from both methods show that the motion parameters are estimated within 10% absolute error, the first method performs the motion compensation in the time domain and does not require frequency-domain data pre-processing, as well as demonstrates generally better results than the second method. The estimated motion parameters are then used to recover the motion-compensated Doppler spectrum from the Doppler spectrum of the antenna on a floating platform, and the results coincide well with the Doppler spectrum of the fixed antenna.

In the next stage of the thesis, a new real-time method is proposed to estimate the significant wave height directly from the antenna's received electric field in the time-domain without requiring prior knowledge of the motion parameters or performing motion compensation. Based on the relation between the ocean surface displacement and the received electric field, this method calculates the significant wave height from the windowed variance of the upper envelope of the received electric field. This method is applied for up to second-order backscatter, and the results are compared with the case when only first-order backscatter is considered, and shows a considerable improvement. A preliminary calibration is required, which can be carried out either by the deployment of a wave buoy or by analyzing the data over a time period during which the sea state varies. The results from this simple proposed technique show that it may be used to estimate the significant wave height with a root-mean-square error (RMSE) of less than 12 cm over a wide range of significant wave height values.

Dedicated to the brave women in Iran whose movement is an inspiration to the world!

Women, Life, Freedom

Acknowledgements

I would like to express my sincere gratitude to my supervisors, Dr. Reza Shahidi and Prof. Eric Gill, for their unwavering support and belief in me. Dr. Shahidi's precious knowledge and technical assistance at every stage of my research project were encouraging and made this path pleasant for me. Prof. Gill's experience, insightful comments, and suggestions trained me to become a thoughtful researcher.

The financial support for this work was provided by Memorial University and the Natural Sciences and Engineering Research Council of Canada (NSERC) through Discovery Grants RGPIN-2020-07155 to R. Shahidi and RGPIN 2020-05003 to E. W. Gill.

I wish to extend my special thanks to our radar group for always being inspiring. I learned a lot from all of you, and spent a very pleasant and rewarding time studying in our lab and living in St. John's.

Finally, I am grateful to my husband and family for always being supportive and encouraging. Without them, this achievement would not have been possible.

Table of Contents

List of Tables

List of Figures

List of Symbols

δ Dirac delta function (p. 17)

$\Delta\omega$ Doppler frequency resolution (rad/s) (p. 20)

$\delta\vec{\rho_0}$ Platform displacement (m) (p. 19)

$\epsilon(\omega)$ Random phase variable as a function of angular frequency (rad) (p. 20)

η Normalized Doppler frequency (p. 16)

Γ_s Electromagnetic and hydrodynamic coupling coefficient (p. 17)

λ_0 Transmitted signal wavelength (m) (p. 20)

ω_B Bragg frequency (rad/s) (p. 16)

ω_d Doppler frequency (rad/s) (p. 16)

ω_p Angular frequency of the platform motion (rad/s) (p. 19)

ϕ Initial direction of the platform motion (rad) (p. 19)

ρ Distance between the transmitter and receiver (m) (p. 19)

ρ_1 Distance between the transmitter and scattering patch (m) (p. 19)

ρ_2 Distance between the receiver and scattering patch (m) (p. 19)

ρ_{01} Distances from the transmitter to the scattering patch (m) (p. 20)

ρ_{02} Distances from the receiver to the scattering patch (m) (p. 20)

$\sigma(\omega)$ Total radar-cross section (p. 20)

σ_1 First-order radar cross section (p. 16)

σ_2 Second-order radar cross section (p. 17)

τ Electrical field travel time (s) (p. 47)

θ_0 Direction of the platform motion (rad) (p. 19)

θ_k Direction of ocean wave vector (rad) (p. 19)

θ_p Direction of the ocean wave vector (rad) (p. 19)

ξ Vertical ocean surface displacement (m) (p. 47)

ξ_s Scaling factor (p. 50)

a Amplitude of the platform motion (m) (p. 19)

BW System's bandwidth (Hz) (p. 20)

c Speed of light in a vacuum (m/s) (p. 37)

$E(t)$ Electric field (V/m) (p. 20)

$E_{0_n}^+$ Normal component of the received electric field (V/m) (p. 47)

f Frequency (Hz) (p. 47)

G_r Receiver gain (p. 20)

G_t Transmitter gain (p. 20)

H_s Significant wave height (m) (p. 10)

$J_0(z)$ Zeroth-order Bessel function of the first kind (p. 20)

K Normalized wavenumber (p. 16)

k_0 Radar wave number (1/m) (p. 16)

n Order of Bessel function (p. 19)

P_t Power of transmitter (W) (p. 20)

$R(t)$ Autocorrelation function (V^2) (p. 20)

r Distance between the transmitter and receiver to the scattering patch in monostatic configuration (m) (p. 47)

$S(K, \theta)$ Spatial ocean wave spectrum ($m^2 s$/rad) (p. 16)

t Time (s) (p. 19)

$W(.)$ Weighting function (p. 50)

List of Abbreviations

CC correlation coefficient (p. 56).

DOF degrees of freedom (p. 5).

HF high frequency (p. 1).

HFSWR high frequency surface wave radar (p. 1).

OW orthogonal weighting (p. 8).

RCS radar cross-section (p. 4).

RF radio frequency (p. 9).

RMSE root mean square error (p. 41).

STAP space-time adaptive processing (p. 6).

Chapter 1

Introduction

1.1 Research Rationale and Objectives

Ocean wave information measurement is essential for numerous marine applications, including marine forecasts, vessel navigation, and many ocean engineering projects. High frequency surface wave radar (HFSWR) is a type of remote-sensing device that has great capability to help provide this information. High-frequency (HF) radar operates in the HF band (3-30 MHz), corresponding to a 10-100 m wavelength. This property enables efficient surface propagation, and as a consequence, a large detection range of a few hundreds of kilometers may be obtained [1]. The transmitted signal reacts strongly with the ocean surface, which is highly conductive at these frequencies, and the received signal contains ocean surface information. Figure 1.1 shows the HFSWR owned by Memorial University, which is located at Argentia, Newfoundland and Labrador. An example of the Doppler spectrum calculated from the received signal of this antenna is depicted in Figure 1.2.

With the development of HFSWR applications in remote sensing of the ocean surface, one possible configuration is to mount the radar on a floating ocean platform, such as an oil exploration platform. Accurate wave measurements obtained from offshore platforms serve a crucial role in design considerations, operational safety, and overall efficiency. Deploying and maintaining measurement devices in the water can be expensive, underscoring the attractiveness of utilizing platform-mounted remote-sensing systems [2]. In this situation, the platform motion considerably affects the

(a)

(b)

Figure 1.1: HFSWR at Argentia, Newfoundland a) transmitter array consisting of two elements, b) receiver array consisting of 12 elements.

Doppler spectrum of the ocean as received by the radar. Extracting ocean surface wave and current parameters from fixed HF radar Doppler spectra is a well-established practice. Calculating the motion-compensated Doppler spectrum and data extraction from the received motion-contaminated signal of the antenna on a floating platform are new challenges that have only been studied significantly in recent years.

When an HF radar is mounted on a floating platform, the platform's motion will

contaminate the radar Doppler spectrum, and this results in the extracted ocean surface information being inaccurate [3]. Platform motion will induce some symmetrical peaks in the antenna Doppler spectrum. Also, compared to the spectrum obtained when the antenna is fixed, the Bragg peaks in the spectrum obtained from an antenna on a sinusoidally floating platform have their energy spread out over a broader frequency band.

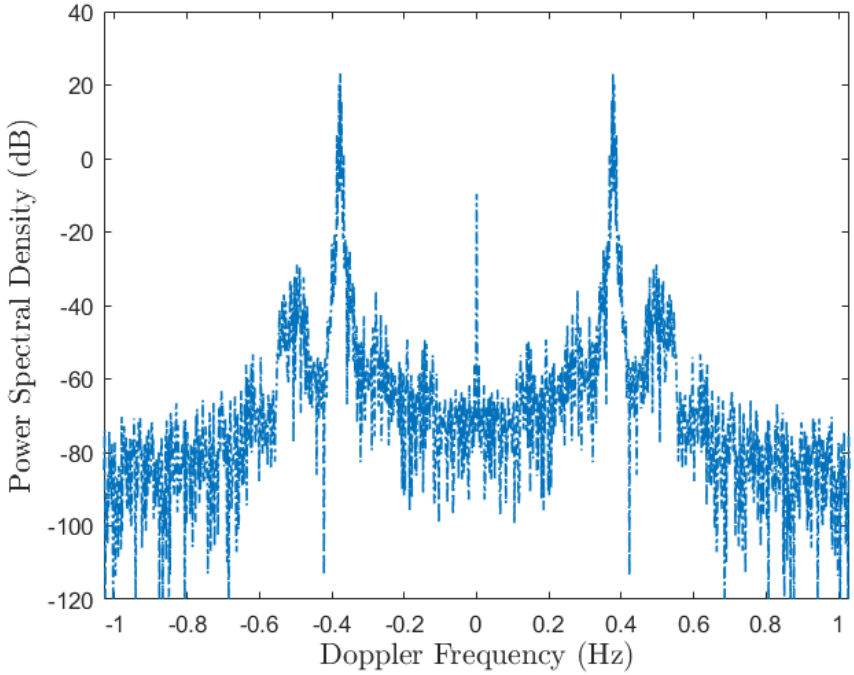

Figure 1.2: An illustration of Doppler spectrum drawn from HFSWR data acquired at Argentia, Newfoundland.

Motion compensation methods have thus far been mainly based on known motion parameters (including amplitude and angular frequency of the motion) [4, 5]. Since motion parameters are obtained from sensors, measurement errors and time delays will affect their integrity. Therefore, it is valuable to develop a technique to find the motion parameters directly from the received motion-contaminated radar signal and use these estimated motion parameters to compensate for the effect of motion on the radar Doppler spectrum.

In this study, motion compensation of the Doppler spectrum from an HF surface wave radar on a floating platform is investigated when the platform motion parameters are not known *a priori*. Two methods for platform motion parameter estimation

are presented in this thesis. Assuming the platform moves according to a single-frequency sinusoidal motion model, it was shown in [5] that the radar cross-section (RCS) of the antenna on a floating platform could be obtained by multiplying the ocean RCS for the case of the fixed antenna by a motion factor which is a zero-order Bessel function of the first kind [5]. The argument of the Bessel function is determined by the motion parameters. The first method uses the zeros of the motion factor in the autocorrelation function of the received electric field from the floating antenna to calculate the motion parameters. The second method estimates the motion parameters based on the relationship between Doppler frequency and amplitude of the motion-induced peaks and platform motion parameters. Then, the estimated motion parameters are applied in the motion compensation technique [5] to obtain the motion-compensated Doppler spectrum.

In addition, it has been shown that by considering up to second-order backscatter, there is a quadratic relation between the received electric field and the vertical ocean surface displacement. A new significant wave height extraction method from an antenna on a floating platform is proposed, which calculates the significant wave height from the windowed variance of the upper envelope of the electric field. The distinctive feature of this method is that the significant wave height is extracted from the received electric field without preliminary data processing. This technique does not require motion compensation, Doppler spectrum formation, or knowledge of motion parameters.

1.2 Literature Review

1.2.1 Motion Compensation

Platform-mounted high-frequency radars have been widely studied to discover the effects of platform motion and propose methods for suppressing motion effects on extracted data. For example, Walsh *et al.* [3, 6] derived the first- and second-order RCSs for an antenna on a platform moving sinusoidally in a monostatic configuration. Monostatic refers to the configuration where the transmitter and receiver are collocated, or the distance between the transmitter and receiver is very small compared to the distance to the expected scattering patch. The effect of the platform motion

was shown to be manifested as symmetrical peaks in the Doppler spectrum around the Bragg peaks, as can be seen in Figure 1.3. Also, compared to the spectrum of the fixed antenna, the energy of the Bragg peaks in the spectrum of an antenna on a sinusoidally-moving platform is distributed over a wider frequency range.

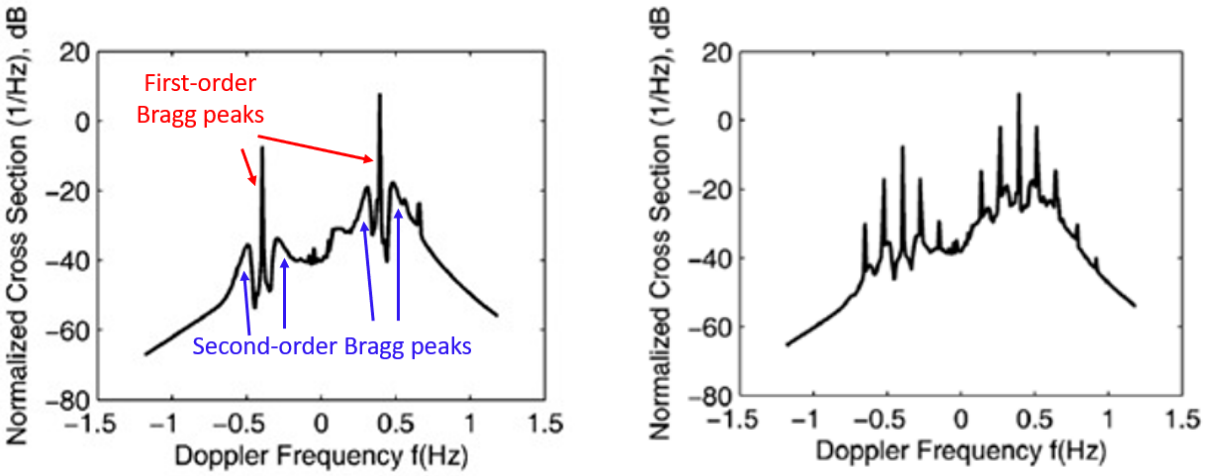

(a) (b)

Figure 1.3: An example of the radar cross-section of a) a fixed antenna, b) an antenna on a floating platform [3].

The bistatic first- and second-order RCSs for the case of dual-frequency platform motion were presented in [7–9]. The bistatic configuration refers to the case where the distance between the transmitter and receiver is comparable to the distance to the scattering patch. For the pitch and roll motion of the platform, first- and second-order RCSs were derived in [10]. It was discovered that this motion model has the same effect of frequency modulation as horizontal motions. When the amplitude of the motion increases, the magnitude differences between motion-induced and Bragg peaks decrease.

For the case of a shipborne HF radar, the first-order RCS was obtained for a monostatic configuration assuming a rotational motion model in [11] and a horizontal motion model in [12]. Also, expressions for the RCS consisting of the first-order and second-order components for the monostatic and bistatic configurations were derived in [13] and [14], respectively. The motion model was assumed to include six degrees-of-freedom (DOF), including yaw, pitch, roll, heave, sway, and surge (See Figure 1.4). While the effect of the motion on shipborne HFSWR is the same as that for an antenna

on a floating platform, the second-order spectrum is most impacted by yaw [13], so the antenna should be positioned near the center of rotation to minimize the motion's effect.

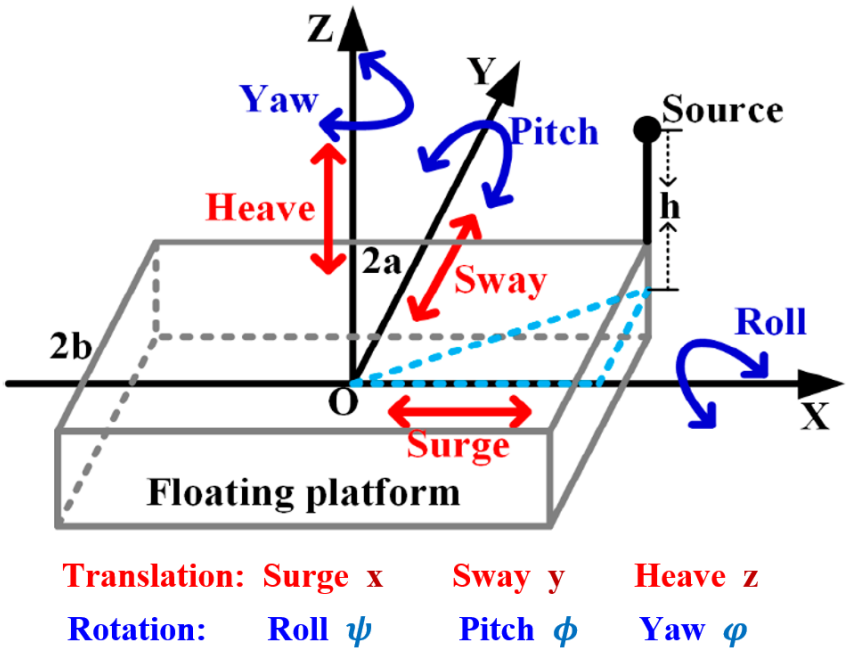

Figure 1.4: An illustration of the shipborne HFSWR platform with six degrees of freedom (DoF) of motion [12]. The transmitter antenna is placed at (a, b, h).

During the past two decades, various approaches have been proposed to solve the platform motion effect issue:

- Motion compensation based on recovery from the motion-contaminated Doppler spectrum
- Motion compensation based on the recovery of the antenna pattern and array steering vector
- Methods using space-time adaptive processing (STAP) for motion compensation
- Motion parameter estimation for performing the motion compensation (when motion parameters are previously unknown).

Motion-Compensation Methods Based on Recovery of the Contaminated Doppler Spectrum

One method to compensate for the effect of platform motion on Doppler spectra is to recover the motion-*compensated* Doppler spectrum from the motion-*contaminated* Doppler spectrum. In this method, the motion-induced peaks will be removed from the Doppler spectrum, and the energy and the bandwidth of the first- and second-order peaks will be recovered. Then the ocean surface information can be extracted from this spectrum. Gill *et al.* [4] established a relation between the RCS of the ocean for the case of the antenna on a floating platform with that when the antenna is fixed in order to compensate for dual-frequency platform motion effects on the Doppler spectra.

It was found that Doppler spectra can be recovered by deconvolving the radar data with a transfer function. Four different deconvolution methods were examined in that paper, and it was found that the iterative Tikhonov regularization deconvolution method gives superior results to the other methods discussed. The shortfall of this technique is that the transformation matrix could become ill-conditioned, and the results were inaccurate in the presence of high levels of noise. This relation was simplified considerably in [5] by using properties of the Bessel function of the first kind. A new expression for motion compensation in the time domain was derived, which easily expresses the motion effects by the product of the zeroth-order Bessel functions of the first kind. This method accurately recovered the motion-contaminated spectrum, even for noise data. The main limitation of these methods in the literature is that the motion parameters, including amplitude and frequency of the motion, needed to be previously known.

Motion Compensation Methods Based on the Recovery of the Antenna Pattern and Array Steering Vector

The second method for reducing platform motion effects is to recover the radiation pattern and array steering vector of the HFSWR. Wang *et al.* [15] developed a time-varying steering vector model for a phased-array radar system. The maximum likelihood motion compensation technique was applied to the sensor array's received data to suppress sea clutter and improve target detection. The authors considered six

oscillatory motions along with the forward motion for the moving platform. It was concluded platform motions other than forward motion did not affect the Doppler spectrum. The motion compensation method showed robust results to yaw measurement error, and the errors of other motions were assumed to be negligible, assuming a 10% error is considered acceptable.

An array antenna was used in [16], where each array element was mounted on a buoy. As a result, each array element underwent a different movement. A method for compensating for the swell motion effect on the antenna radiation pattern was presented. Locations of the radiation pattern nulls were changed due to the buoy's movement. The disturbance caused by swell motion was corrected by using Schelkunoff's zero placement method [17]. In order to optimize the antenna radiation pattern, the authors subsequently proposed a real-time motion compensation method [18]. This method considered both horizontal and vertical movements. Modifying the coupling matrix and forcing the nulls in the motion-contaminated radiation pattern corrected the vertical and horizontal displacements. These motion compensation methods focus only on retrieving the radiation pattern, whereas the platform motion will also affect the Doppler spectrum.

Space-Time Adaptive Processing

Space-time adaptive processing (STAP) was presented in [19] to suppress the spreading of the Bragg and motion-induced peaks in the Doppler spectra of a ship-borne radar. The spreading of the first-order Bragg peaks was reported to be related to the ship velocity. The spreading spectrum was found to be low pass when the ship velocity is high; otherwise, it is bandpass. In [20], an improved orthogonal weighting algorithm was combined with the sea clutter suppression method in the Doppler domain to enhance the target-detection performance in both the Doppler and spatial domains. The reported results show that this method is more effective than orthogonal weighting (OW) and the two-dimensional fast Fourier transform along with digital beamforming. The STAP method considers the effects of linear motion, whereas [4, 5] apply the compensation for sinusoidal functions. Additionally, the STAP approach is unsuitable for ocean remote sensing applications since it suppresses the sea clutter information in the Doppler spectrum by removing the clutter rather than correcting for it.

Methods based on motion parameter estimation

Zhu *et al.* [21] proposed a method to determine the motion parameters of a ship-borne HFSWR with six-degree-of-freedom motion by using a reference radio frequency (RF) signal transmitted artificially from the coast. Based on the estimated motion parameters, motion compensation was performed using the first-order RCS of the ocean. The pattern search method was implemented to enhance the precision of the amplitude and angular frequency of the motion because high accuracy of the angular frequency is required for good motion compensation. It was mentioned that the results of this method are better than the motion compensation methods performed by motion parameters obtained from sensors. A dual-referenced RF signal is also applied in [22] for motion compensation, while the motion parameters are assumed to be dynamic and include six degrees of freedom. It was shown that this method is capable of compensating for modulation due to random motion.

Since the locations and intensities of the Bragg peaks and motion-induced peaks are a function of the motion parameters, Hashemi *et al.* [23] presented an optimization method to find the motion parameters. Then motion compensation was performed based on the total RCS using the estimated motion parameters. A dual-frequency platform motion was assumed in that paper. The optimization is performed in MATLAB® [24] using the lsqnonlin command. The proposed motion compensation methods were analyzed on synthetic data because of the lack of field data for an HF radar on a floating platform.

In [25], the echo spectrum of the moving target and a motion compensation method was explored for an antenna deployed on a ship. Yaw and forward motion of the ship were considered in this study, and it was shown that the target echo would shift and broaden, and false target echo peaks would be observed. The motion compensation was done in two steps; first, for non-uniform motion by finding the compensated steering vector, and then for the effect of yaw. It was discussed that a precise measurement of the heading is required for accurate target detection and motion compensation.

1.2.2 Significant Wave Height Estimation

Wave measurements provided by an HF surface wave radar on a floating platform such as an oil exploration platform are important for design, safety, and efficiency

reasons [2]. However, the motion of the platform will contaminate the received antenna signals, resulting in inaccurate extracted ocean information. Therefore, a motion compensation method should be applied (discussed in the previous subsection) to recover the Doppler spectrum. After retrieving the Doppler spectrum, an additional stage of processing the Doppler spectrum is required to extract wave information.

It was primarily proposed by Hasselmann [26] that second-order Doppler peaks are proportional to the wave height nondirectional spectrum; therefore, it can be interpreted that the mean-square sea wave height could be calculated from the area under the second-order peaks. Barrick [27] showed that significant wave height could be estimated by a closed-form approximation, namely the ratio between the energies of the second-order and the first-order radar cross sections (RCSs) (See Figure 1.3(a)). An inversion algorithm for ocean wave spectra measurement and subsequently significant wave height estimation was presented by Howell et al. in [28]. In this numerical method, the second-order RCS's integral equation was inverted by approximating the integral to the matrix equation using truncated Fourier series and finding the best fit for the kernel matrix. This technique is suitable for near real-time ocean surface extraction and is able to estimate the significant wave height by the absolute error of 33 cm compared with buoy measurements. Heron et al. compared three different algorithms for significant wave height extraction in [29], all of which are scaled forms of the method of Barrick [27]. It was shown that by using a scaling factor of 0.551, the method of Barrick gave the best results for significant wave heights between 0.1 and 0.7 m.

The first-order Bragg peaks were used in [30] to estimate the significant wave height (H_s). This method is based on the dependence of the non-directional wave spectrum on the wind speed and uses nonlinear fitting to discover the relation between H_s and the value of the non-directional wave spectrum at the Bragg frequency (ω_B). In [31], a model was suggested for wide-beam dual-frequency radars, which estimates values of H_s from the first-order Doppler spectrum. It was theoretically demonstrated that the values of H_s could be determined from the ratio of the first-order spectral powers associated with two radar frequencies, and H_s was calculated using an algorithm that used beamforming and direction finding. The value of H_s could also be obtained from the ratio of the powers of the second-order harmonic peak at $\sqrt{2}\omega_B$ and the Bragg peak through a H_s-mapping algorithm [32].

A nonlinear-optimization based method was presented in [33], which first extracted the directional ocean spectrum from which H_s was obtained. In [34], a method was proposed for obtaining the non-directional wave spectrum from radar data using wave inversion. In addition, by modeling the current variations through the beam, an approach for extracting the non-directional ocean spectrum was developed in [35]. The non-directional wave spectrum was then integrated to calculate H_s. In addition, neural networks can be applied in the inversion process to calculate wave parameters from the directional wave spectrum [36]. However, it was stated in [36] that training the neural networks is time-consuming and resource-intensive, and the neural-network based inversion method fails to incorporate radar beam angle successfully.

Two approaches were proposed in [37], which did not require the calculation of the Doppler spectrum to determine H_s and instead computed H_s directly from the received time series acquired from a stationary HFSWR radar. First-order scatters and the hydrodynamic component of the second-order scatters were considered in that paper. In the two methods presented in [37], the variance of the short-time Fourier transform coefficient and the variance of the first-order received electrical field were used, respectively, to determine H_s. This method was further developed for second-order scatters in [38] to consider the 2^{nd} order electromagnetic component as well.

These previous significant wave height estimation methods are statistically compared in Table 1.1. As can be observed from the Table, the time-domain method presented in [37] has the best ability to estimate H_s accurately. In the current study, the time-domain method in [39] for the first-order scatters, and the approach in [38] for the second-order scatters are both used to estimate H_s from the signal received from a transmitter on a floating platform. This technique bypasses motion compensation and does not rely on prior knowledge of antenna motion parameters (amplitude and angular frequency of the motion).

1.3 Structure of the Thesis

This thesis is organized as follows: Chapter 1 contains the research rationale and objectives, literature review, and thesis organization. Chapter 2 consists of a summary of the background theory for synthesizing the HF radar data. In Chapter 3, two new methods for motion parameter (amplitude and angular frequency of the

Table 1.1: Statistical comparison of significant wave height estimation methods

No.	**TX frequency (MHz)**	H_s **(m)**	**RMSE (m)**	**Ref.**
1	13	0.2-4.5	0.59	[30]
2	7.5-13.5	0.3-2	0.3-0.5	[31]
3	13	0.5-3.5	0.33-0.77	[32]
4	13.38	0.5-4.5	0.61	[33]
5	7.5-25	0.5-9	0.67	[34]
6	8.26	0.5-5	0.51	[35]
7	12.3	1-6	0.46-1.49	[36]
8	13.38	0.5-4.5	0.25-0.41	[37]

motion) estimation and motion compensation of the HFSWR on a floating platform are described; the first is implemented in the time domain, while the other is in the frequency domain, and the results of applying these two methods are presented. Chapter 4 includes a proposed method for H_s extraction from the data received from an antenna on a floating platform and its results. There is no need to know the parameters of platform motion prior to using this technique since it bypasses motion compensation. Finally, in the last chapter, conclusions are drawn.

The thesis contributions have been published or submitted for review in the following journals and presented at the following conferences.

1. *Extraction of the Significant Wave Height from Received High-Frequency Radar Data from an Antenna on a Floating Platform*, **Sepideh Hashemi**, Reza Shahidi, and Eric W. Gill, IET Radar, Sonar and Navigation (2023) (Submitted).

This paper presents a method for estimating the significant wave height from up to second-order received signal when the antenna is mounted on a floating platform. (Chapter 4)

Authors' Contributions:

Sepideh (Seyedehsepideh) Hashemi: Formal analysis; Investigation; Methodology; Software; Validation; Visualization; Writing – original draft.

Reza Shahidi: Conceptualization; Data curation; Funding acquisition; Project administration; Resources; Supervision; Validation; Writing – review and editing.

Eric W. Gill: Funding acquisition; Resources; Supervision; Validation; Writing – review and editing.

2. *Significant Wave Height Estimation from Received High-Frequency Radar Data from an Antenna on a Floating Platform*, **Sepideh Hashemi**, Reza Shahidi, and Eric W. Gill, 31st Annual Newfoundland Electrical and Computer Engineering Conference, St. John's, Canada, November 2022, pp. 1-4.

This paper presents a method for estimating the significant wave height from first-order received signal when the antenna is mounted on a floating platform (Chapter 4).

Authors' Contributions:

Sepideh (Seyedehsepideh) Hashemi: Formal analysis; Investigation; Methodology; Software; Validation; Visualization; Writing – original draft.

Reza Shahidi: Conceptualization; Data curation; Funding acquisition; Project administration; Resources; Supervision; Validation; Writing – review and editing.

Eric W. Gill: Funding acquisition; Resources; Supervision; Validation; Writing – review and editing.

3. *Blind time-domain motion compensation for synthetic Doppler spectra obtained from an HF-radar on a moving platform*, **Sepideh Hashemi**, Reza Shahidi, and Eric W. Gill, IET Radar, Sonar and Navigation (2022) (Published).

This paper includes a time-domain motion compensation method for an antenna on a floating platform. (Section 3.2)

Authors' Contributions:

Sepideh (Seyedehsepideh) Hashemi: Formal analysis; Investigation; Methodology; Software; Validation; Visualization; Writing – original draft.

Reza Shahidi: Conceptualization; Data curation; Funding acquisition; Project administration; Resources; Supervision; Validation; Writing – review and editing.

Eric W. Gill: Funding acquisition; Resources; Supervision; Validation; Writing – review and editing.

4. *Platform motion parameter estimation from synthetic high-frequency radar data*, **Sepideh Hashemi**, Reza Shahidi, and Eric W. Gill, 30th Annual Newfoundland Electrical and Computer Engineering Conference, St. John's, Canada, November 2021, pp. 1–4.

This paper describes a frequency-domain method for estimating motion parameters and motion compensation. (Section 3.3 with the improved results)

Authors' Contributions:

Sepideh (Seyedehsepideh) Hashemi: Formal analysis; Investigation; Methodology; Software; Validation; Visualization; Writing – original draft.

Reza Shahidi: Conceptualization; Data curation; Funding acquisition; Project administration; Resources; Supervision; Validation; Writing – review and editing.

Eric W. Gill: Funding acquisition; Resources; Supervision; Validation; Writing – review and editing.

Chapter 2

Theoretical Background

2.1 Introduction

By utilizing HFSWR, the scattering of waves can be observed, both in terms of first-order and second-order scattering phenomena. Bragg resonant scattering is the principal phenomenon behind the scattering of radio waves from the ocean surface [1]. In general, ocean waves consist of waves with various wavelengths and propagation directions. But, only backscattered echoes from waves traveling toward or directly away from the radar will be significant. Ocean surface waves are dispersive, which means their velocity depends on the wavelength. As a result, there will be two prominent peaks in the Doppler spectrum of the antenna, which are associated with the negative and positive Doppler shifts for approaching and receding waves; these two peaks are defined as first-order Bragg peaks and are shown in Figure 1.3a. The first-order peaks are associated with a first-order (single) scatter. The smaller magnitude to the right and left of the first-order peaks are higher-order Bragg peaks (second-order and greater) which are the effect of multiple scatters of the transmitted wave from the ocean surface (see Figures 1.2 and 1.3a). The analysis of wave spectra derived from HFSWR data helps to understand the dynamics of the ocean surface and has applications in areas such as oceanography, coastal monitoring, and maritime operations.

This chapter discusses the method for generating synthetic HF radar data for motion compensation and the H_s estimation methods proposed in this thesis. In the first two sections, the first- and second-order RCSs for the case of a fixed antenna and

the case when the antenna is mounted on a floating platform are presented. In the next section, the procedures to calculate the antenna's received electric field and the resulting Doppler spectrum are presented. A summary of the chapter is given in its final section.

2.2 Radar Cross-Section of the Fixed Antenna

The proposed methods were tested on synthetic data because of the lack of available measured field data from an HF radar on a floating platform. In the first step, first- and second-order RCSs, in dimensionless form which is normalized to the area of the surface patch, for the fixed antenna were simulated. This is achieved by defining the normalized variables,

$$\text{Normalized water depth} : D = 2k_0 d \tag{2.1}$$

$$\text{Normalized wavenumber} : K = k/2k_0 \tag{2.2}$$

$$\text{Normalized Doppler frequency} : \eta = \omega_d/\omega_B \tag{2.3}$$

where d, k, k_0 are the unnormalized water depth, unnormalized ocean wavenumber, and radar wavenumber, respectively. Variables ω_d and $\omega_B = \sqrt{2gk_0}$ are Doppler and Bragg frequencies, respectively, and g is the acceleration due to gravity. The normalized first-order RCS ($\sigma_1(\eta)$) calculated from the first-order scatter can be obtained from Equation (2.4) [40, 41]

$$\sigma_1(\eta) = 4\pi \sum_{m=\pm 1} S(1, (1+m)\pi/2)\delta(\eta - m) \tag{2.4}$$

where S is the spatial ocean wave spectrum which is a function of normalized wavenumber K and α, the direction of the ocean wave vector $m\mathbf{K}$. For the Bragg peaks, $K = 1$ and α is set to $(1+m)\pi/2$, where $m = \pm 1$. δ is the Dirac delta function.

The normalized second-order radar cross-section ($\sigma_2(\eta)$) can be calculated from

Equation (2.5) [40, 41]

$$\sigma_2(\eta) = 8\pi \sum_{m,m'=\pm 1} \int_{-\pi}^{\pi} \int_{0}^{\infty} |\Gamma_s|^2 S(K,\alpha) S(K',\alpha') \delta\left(\eta - m\sqrt{K_D} - m'\sqrt{K'_D}\right) K dK d\theta \tag{2.5}$$

where

$$K_D = K \tanh(KD) \tag{2.6}$$

$$K'_D = K' \tanh(K'D) \tag{2.7}$$

Γ_s denotes the sum of the electromagnetic [42] and hydrodynamic [43] coupling coefficients. The variable θ represents the radar look direction. The variable $\alpha^{'}$ denotes the direction of the wave vectors $m^{'}\mathbf{K}^{'}$, where $m^{'} = \pm 1$. $S(K,\alpha)$, the spatial ocean wave spectrum, can be modeled as the product of two separate factors, the non-directional spectrum $f(K)$ and directional wave spectrum $g(s,\alpha)$. The variable s is the spreading factor which is assumed to be 2. The Pierson–Moskowitz model was used for the non-directional term [44], and the directional factor was described by a cosine-power law [45].

$$S(K,\alpha) = f(K)g(s,\alpha) \tag{2.8}$$

$$f(k) = \frac{0.0081}{2k^4} e^{\frac{-0.74g^2}{k^2U^4}} \tag{2.9}$$

$$g(s,\alpha) = \frac{2^{2s-1}}{\pi} \frac{\Gamma^2(s+1)}{\Gamma(2s+1)} \cos^{2s}\left(\frac{\alpha - \alpha^*}{2}\right) \tag{2.10}$$

where Γ represents the gamma function and U is the wind speed at height 19.5 m above the mean sea surface, and α^* denotes the dominant direction of the wavefield.

Using Equations (2.11) and (2.12) below, the normalized RCSs ($\sigma_1(\eta)$ and $\sigma_2(\eta)$) can be converted to RCSs in terms of the Doppler frequency ($\sigma^1(\omega_d)$ and $\sigma^2(\omega_d)$).

$$\sigma_1(\eta) = \omega_B \sigma^1(\omega_d) \tag{2.11}$$

$$\sigma_2(\eta) = \omega_B \sigma^2(\omega_d) \tag{2.12}$$

2.3 Radar-Cross Section of the Antenna on a Floating Platform

Figure 2.1 shows the general ocean patch scatter, and Figure 2.2 illustrates the general first-order monostatic scatter geometry with antenna motion. It is assumed that the transmitter antenna is floating and the receiver antenna is fixed. This configuration can be used for conditions when there is insufficient space for both transmitter and receiver on the shore. Also, installing the transmitter antenna on the moving platform like a buoy, it can move and cover a larger area.

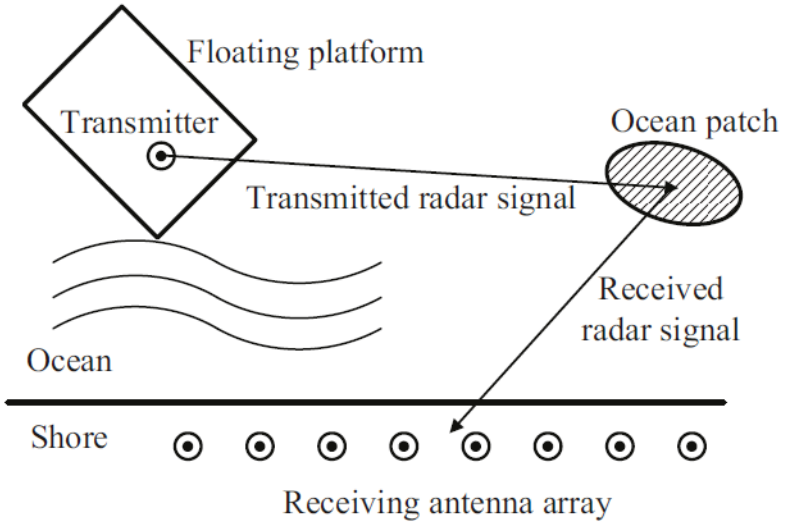

Figure 2.1: An illustration of ocean patch scatter for a fixed receiver and a floating transmitter case [9]

The origin is taken to be the transmitter location, and the transmitted signal is scattered by the ocean surface at the point (x, y). ρ_1 and ρ_2 are the distances between the transmitter and receiver, respectively, to the scattering patch, and ρ is the distance between the transmitter located at the origin and the receiver. The small displacement of the platform on which the transmitter is deployed is denoted by $\delta\vec{\rho_0}$, and θ_0 is the direction of the platform motion.

For the purposes of this thesis, the platform motion model is reduced to a single frequency, but in general, it will contain multiple frequencies. In this regard, the displacement model of the platform can be expressed as [3]

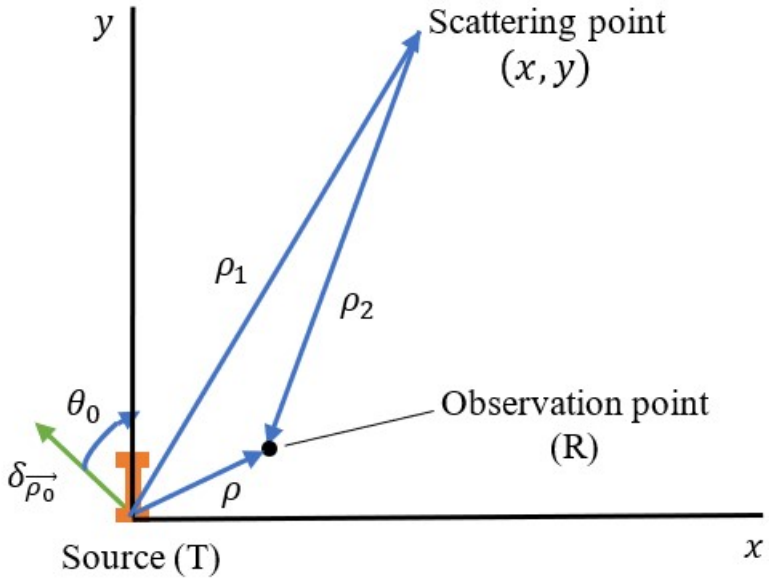

Figure 2.2: General first-order monostatic scatter geometry with antenna motion. ρ is very small compared to ρ_1 and ρ_2.

$$\delta\vec{\rho_0}(t) = [a\cos(\omega_p t + \phi)]\hat{\rho}_p \tag{2.13}$$

where a, ω_p, and ϕ are the amplitude, radian frequency, and the initial phase of the cosine function, modeling the single-frequency platform motion, respectively.

For the dual-frequency platform motion model, Gill *et al.* [4] established a relation between the radar cross-sections for an antenna on a floating platform and the fixed-antenna case. For single-frequency platform motion, this relation can be reduced to

$$\sigma_{floating}(t) = \sigma_{fixed}(t) \cdot \sum_{n=-\infty}^{\infty} J_n^2(z) e^{-jn\omega_p t}. \tag{2.14}$$

$\sigma_{floating}$ and σ_{fixed} are the total RCS (including the first-order and second-order RCSs) for the case of the antenna on a floating platform and the fixed-antenna case, respectively, and J_n is the n^{th}-order Bessel function of the first kind. For the monostatic configuration

$$z = 2ak_0\cos(\theta_k - \theta_p) \tag{2.15}$$

where θ_k is the direction of the ocean wave vector, and θ_p denotes the platform direction of motion in x-y plane.

In [5], Equation (2.14) was simplified considerably by using properties of the Bessel function of the first kind, and a new expression for motion compensation in the time domain was derived. Equation (2.16) shows that the radar cross-section of the antenna on a floating platform can be obtained simply by multiplying the radar cross-section of the fixed antenna by a motion factor which is the zeroth-order Bessel function of the first kind:

$$\sigma_{floating}(t) = \sigma_{fixed}(t) \cdot J_0(2z \sin(\omega_p t/2)). \tag{2.16}$$

2.4 Received Electric Field and Doppler Spectrum

The received electric field of the fixed antenna can be calculated from Equations (2.17), and (2.18) [46] as

$$E(t) = \sqrt{\frac{M}{\Delta\omega}} \int_{BW} e^{i\omega t} e^{j\varepsilon(\omega)} \sqrt{\sigma(\omega)\frac{d\omega}{2\pi}} \tag{2.17}$$

where

$$M = \frac{\lambda_0^2 G_r G_t P_t}{(4\pi)^3 \rho_{02}^2 \rho_{01}^2} F^4(\omega_0). \tag{2.18}$$

λ_0 is the transmitted signal wavelength, ω_0 is the radial frequency of the transmitted signal, G_r, G_t, and P_t denote the receiver gain, transmitter gain, and the power of the transmitter, respectively. The variables ρ_{01} and ρ_{02} represent the distances from the transmitter and receiver to the center of the scattering patch, respectively. $\Delta\omega$ is the angular Doppler frequency resolution, $F(\cdot)$ represents the Sommerfeld attenuation function, $\sigma(\omega)$ is the total RCS, $\varepsilon(\omega)$ represents a random phase variable that is uniformly distributed between 0 and 2π, and BW is the system's bandwidth. When an antenna is mounted on a floating platform, not only is the received signal frequency modulated by the platform motion, but it should be considered that external noise is also modulated by platform motion because of the limited bandwidth [4].

The Doppler spectrum of the signal may be obtained as in from [4] from

$$P(\omega) = \frac{1}{\Delta t} \left| \int_{t_1}^{t_2} R(t) e^{-j\omega t} dt \right|^2 \tag{2.19}$$

where $R(t)$ is the autocorrelation function of the received signal, and $\Delta t = t_2 - t_1$ is the duration of the time-series.

2.5 Chapter Summary

In this chapter, the theoretical background, which is applied to generate synthetic HF radar data for the proposed method, is presented. The radar configuration is taken to be monostatic, in which the distance between the transmitter and receiver is very small compared to the distance of the scattering patch to the receiver and to the transmitter, with a floating transmitter and a fixed receiver. The equations presented in this chapter assume a single-frequency platform motion model. As shown in [5], the motion compensation can be performed by dividing the RCS of the antenna on a floating platform by a motion factor (zeroth-order Bessel function of the first kind) and the autocorrelation of the antenna on a floating platform is obtained by the product of the autocorrelation of the received electric field of a fixed antenna and motion factor. The procedures to find the received electric field and the Doppler spectrum were also described.

Chapter 3

Blind Motion Compensation of Data from an Antenna Mounted on a Floating Platform

3.1 Introduction

In order to extract target and ocean information from high-frequency surface wave radar (HFSWR) data when the radar is mounted on a floating platform, motion compensation of the received signal may first be performed, and then the information can be estimated from the resulting motion-compensated signal (See Figure 3.1). Two techniques for motion compensation of the radar Doppler spectrum are presented when the motion parameters (including the amplitude and angular frequency of the motion) are not known *a priori*. The first method is a new approach for obtaining the motion parameters from the time-domain autocorrelation of the received electric field of an antenna on a floating platform. The locations of the zeros of the autocorrelation function of the received signal are utilized to estimate the motion parameters. In addition, since the frequencies and intensities of the Bragg peaks and motion-induced peaks in the antenna spectrum are functions of the motion parameters, a technique is proposed in the second method to find the motion parameters from the peak information. A single-frequency platform motion model is assumed in this thesis. The results show that motion parameter values estimated in the motion-compensation process match well with the true motion parameter values, and there is good agreement

between the motion-compensated spectrum and the Doppler spectrum for a fixed antenna.

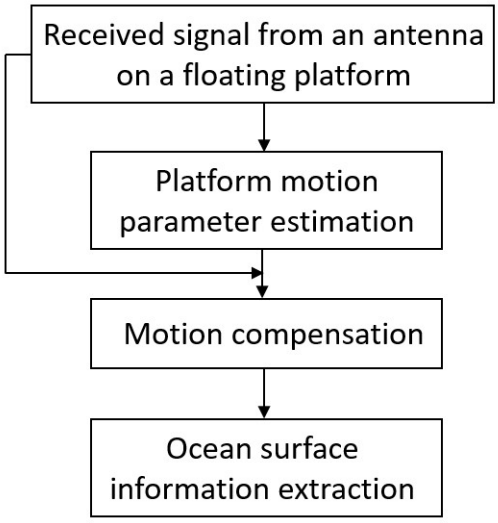

Figure 3.1: Ocean surface parameter extraction method from the motion-compensated received signal from an antenna on a floating platform

In this chapter, techniques for blind motion compensation are introduced. The first motion-parameter estimation method and its results are presented in Section 3.2. The second technique and the simulation results are described in Section 3.3. The final section contains a summary of the chapter and conclusions.

3.2 Method 1: Motion Parameter Estimation Based on Zeros of the Motion Factor

3.2.1 Proposed Solution

The radar cross-section for an assumed range cell is proportional to the Fourier transform of the autocorrelation function of the received electric field [3]. Furthermore, because of the lack of field data for an antenna on a floating platform and to better simulate the experimental data, we calculated the autocorrelation of the received electric field, which consists of the combination of the sea clutter plus external noise [47]. Therefore, the autocorrelation function can be utilized to elucidate the properties of the RCS in the time domain.

The autocorrelation of the received signal of the antenna on a floating platform is calculated by multiplying the autocorrelation of the received signal of the fixed antenna by the motion factor $J_0(2z\sin(\omega_p t/2))$. In this motion factor, J_0 is the zeroth-order Bessel function of the first kind, ω_p and t are angular frequency of platform motion and time, respectively, and z is already defined in Equation 2.15. The autocorrelation of the received signal of the antenna on a floating platform in the time domain is an oscillating function that has zeros at the locations of the zeros of either the RCS of the fixed antenna or the Bessel function of the first kind, as can also be seen in Equation (2.16) for the RCS. The zeroth-order Bessel function of the first kind has an infinite number of zeros, the first few of which are depicted in Figure 3.2 (as may be found, for example, in [48]) and the values of which are given in Table 3.1.

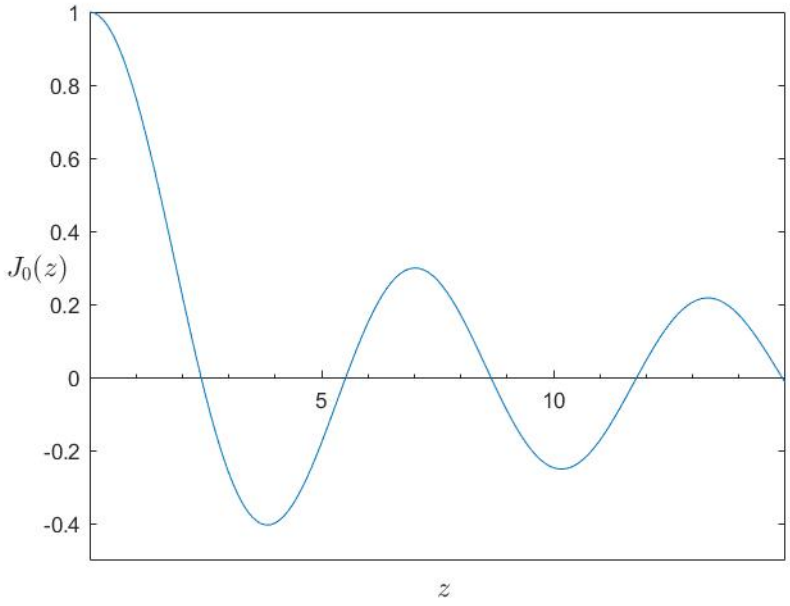

Figure 3.2: Zeroth-order Bessel function of the first kind

Table 3.1: Locations of the first four positive zeros of the zeroth-order Bessel function of the first kind, $J_0(z)$

Index of positive zeros of $J_0(z)$	1	2	3	4
z	2.4048	5.5201	8.6537	11.7915

When the radar ocean surface cross-section for the case of the fixed antenna is multiplied by a zeroth-order Bessel function of the first kind, there will be some

locations with very small fluctuations that correspond to the location of the zeros associated with the zeros of the Bessel function. While the argument of the Bessel function is a function of the amplitude and frequency of the motion, even for the multiple-frequency platform motion model, motion parameters can be easily obtained from the zeros of the Bessel function. These motion parameters can then be used in Equation 3.1 to recover the RCS for the fixed-antenna case. The motion-compensated autocorrelation can be obtained by dividing the autocorrelation of the antenna on the floating platform by the motion factor $J_0(2z\sin(\omega_p t/2))$, obtained from the estimated motion parameters.

$$\sigma_{fixed}(t) = \frac{\sigma_{floating}(t)}{J_0(2z\sin(\omega_p t/2))} \tag{3.1}$$

3.2.2 Simulation and Analysis

The simulations for this stage were performed in MATLAB® [24]. Sample autocorrelations are plotted for different values of frequencies and motion parameters in Figures 3.3 and 3.4. The values obtained by modeling the floating platform with a mooring system are shown in Table 3.2. Also, the parameter set which was used in the simulation process is shown in Table 3.3. The electric field is sampled with a period of 0.0625 s over 900 s.

Table 3.2: Motion parameters used for generation of synthetic Doppler spectrum

No.	**TX frequency (MHz)**	$\boldsymbol{H_s}$ **(m)**	$\boldsymbol{a}$ **(m)**	$\boldsymbol{\omega}$ **(rad/s)**	**Ref.**
1	5	14	10	0.08	E. B. Hanssen [49]
2	10	8	2	0.05	H. Cao *et al.* [50]
3	20	2.05	5.5	0.02	L. Zhang *et al.* [39]
4	25	2.37	1.228	0.127	J. Walsh *et al.* [3]

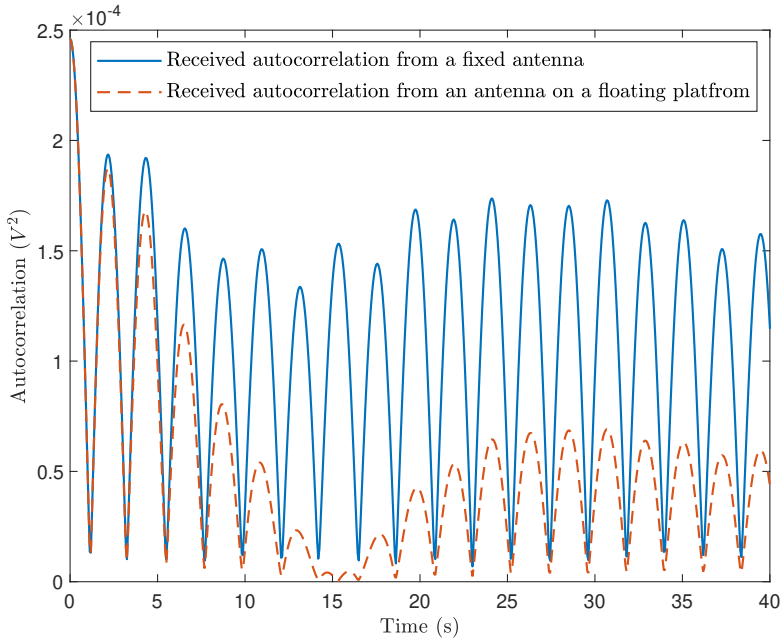

(a)

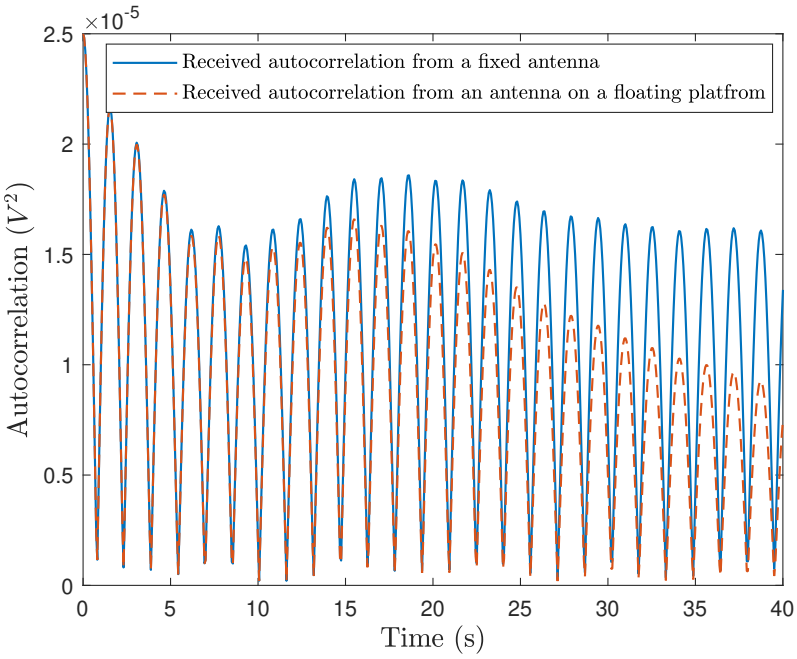

(b)

Figure 3.3: Autocorrelation of the received signal of the antenna on a floating platform in the time domain (a) for motion parameter set no. 1, (b) for motion parameter set no. 2.

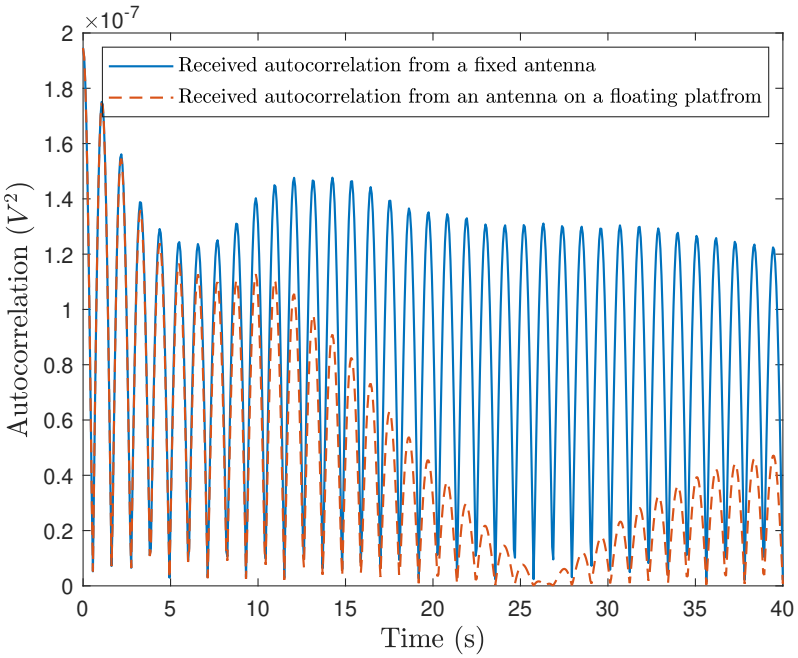

(a)

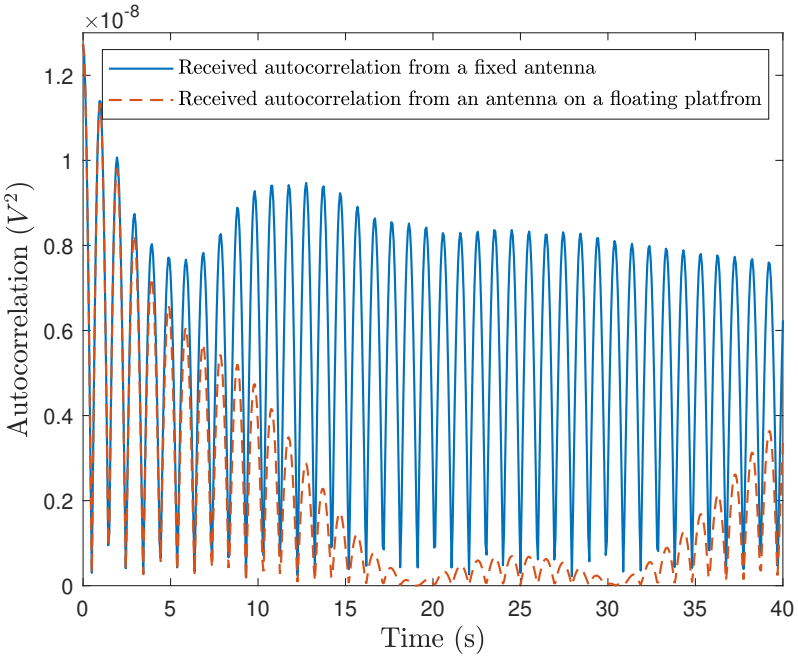

(b)

Figure 3.4: Autocorrelation of the received signal of the antenna on a floating platform in the time domain (a) for motion parameter set no. 3, (b) for motion parameter set no. 4. The signal-to-noise ratio is taken to be 10 dB.

Table 3.3: Parameter set considered in the simulation [47]

Patch width (m)	2500
Direction of platform motion (rad)	0.02
Peak power (kW)	16
Half power beamwidth (rad)	0.07029
Transmitter gain	1.585
Receiver gain	65.76
Distance from path to transmitter and receiver (km)	50
SNR (dB)	10

It is noteworthy to mention that the magnitude of the modulation is bounded by unity, which means the maximum value of the autocorrelation is also restricted. Therefore, for motion compensation, we have to consider a minimum constraint value on the motion factor when dividing the autocorrelation of the received electric field from the antenna on a floating platform by the motion factor (Bessel function).

As shown in Figure 3.3(a), when the motion amplitude is high for a transmission frequency of 5 MHz, there is a zero in the autocorrelation plot, which is associated with the Bessel function. However, for lower amplitude cases, as in cases 1 and 2, the amplitude of the motion should be high enough to reach the zero of the Bessel function in the plot because k_0 limits the argument of the Bessel function (There is no zero related to the Bessel function in Figure 3.3(b)). Nevertheless, when the coefficient of a in the argument of the Bessel function reaches one, then the Bessel function will become $J_0(a)$, which will happen periodically depending on the period of the sine function. $J_0(a)$ will also be the minimum value of the Bessel function for the multiplication obtaining the signal from the transmitter on the floating platform. It will no longer be zero but some other minimum value. Retrieving the motion parameters will be more difficult in this case because there are also zeros from the received non-motion contaminated signal. On the other hand, by increasing the frequency and thus increasing the wavenumber k_0, the zeros of the autocorrelation plots for the lower amplitude would be identifiable (Figures 3.4(a), (b)). It should be noted that the temporal-curve data for both synthetic data in this paper and field data are not initially smooth. A moving average window (11 samples) is applied before taking the autocorrelation to make the values smooth. It is important to highlight that the introduction of noise to the received electric field causes slight shifts in the location

of the zeros of the Bessel function. This factor can potentially impact the accuracy of parameter estimation.

3.2.3 Optimization Process

Because of the nature of the Bessel function, the zeros of the Bessel function in the autocorrelation plots of the antenna on the floating platform occur at the locations where we have oscillations with lower amplitudes; these locations are the points from which we can estimate the motion parameters. For the purpose of clarification, assume that in Figure 3.4(b), the first zero of the Bessel function occurs at t=19.062 s. Any function value lower than 3.16×10^{-12} is assumed to be zero in this figure. By substituting t=19.062 s in the argument of the Bessel function in Equation (2.16) and, given that the location of the first zero of the Bessel function is at 2.4048,

$$2z \sin\left(\frac{19.062\omega_p}{2}\right) = 2.4048. \tag{3.2}$$

Then, z and ω_p can be obtained by using a nonlinear least squares solver in MATLAB® [24], and a is calculated from Equation (2.15). For the multiple-frequency model of the platform motion, multiple zeros of the Bessel functions can be considered to find the motion parameters, though this is not done here.

From the optimization process, the locations of the zeros of the autocorrelation function for the antenna on the floating platform are obtained. These locations and the autocorrelation function are then passed to MATLAB®'s nonlinear least-squares optimization function, the lsqnonlin command [24]. A two-step optimization process was used for accurate estimation of the motion parameters, within which the objective functions were $\mathbf{G_1}$ and $\mathbf{G_2}$ according to Equations (3.3) and (3.4). $\mathbf{G_1}$ was used for the first stage of optimization while $\mathbf{G_2}$ was used for the second stage. The estimated parameters from the first step of the optimization process were passed to the second step, helping to precisely estimate the platform motion parameters and accurately estimate the Doppler spectrum. The vector $\mathbf{t}_z$ corresponds to the positions of the analytical zeros of the autocorrelation function for the antenna on the floating platform. $\mathbf{R}_n$ denotes the motion-compensated autocorrelation function matrix and the $\mathbf{R}_{n0}$ are the $\mathbf{R}_n$ values at the t_m first local minima points, where t_m is set to 1000. $\mathbf{R}_{nf}$ is the maximum value of the autocorrelation function of the electric field of the

antenna on a floating platform, and max() is the maximum value function. To define $\mathbf{G_2}$, the values ($\mathbf{Z}_n$) and indices (**locs**) at which the local minima of $\mathbf{R}_n$ occur, are obtained. Then $\tilde{\mathbf{t}}$, which corresponds to the positions of the analytical zeros of the motion-compensated autocorrelation function, is obtained by finding $\mathbf{t}$(**locs**), where $\mathbf{t}$ denotes time.

$$\mathbf{G_1}(\mathbf{t}) = \epsilon_1 {J_0}^2 \left(2z \sin\left(\frac{\omega_p t_z}{2}\right)\right) + \epsilon_2 \left(\frac{\mathbf{R}'_{n0}(t_m)}{\mathbf{R}_{n0}(t_m)}\right)^2 + \epsilon_3 \max^2(0, |\mathbf{R}_n| - \mathbf{R}_{nf}) \tag{3.3}$$

$$\mathbf{G_2}(\mathbf{t}) = \mu_1 {J_0}^2 \left(2z \sin\left(\frac{\omega_p t_z}{2}\right)\right) + \mu_2 |\mathbf{R}_n| + \mu_3 (\mathbf{Z}_n)^2 + \mu_4 \mathrm{var}^2(\tilde{\mathbf{t}}) \tag{3.4}$$

Also, var denotes the variance of its vector-valued argument. The first term in $\mathbf{G_1}$ is the square of the motion factor, while the second term is applied to make the time difference between the local minima shorter, and the third term has been used to maximize the difference between the motion-compensated autocorrelation and the autocorrelation function associated with the antenna on a floating platform. In $\mathbf{G_2}$, the second term is used to minimize the motion-compensated autocorrelation function, $\mathbf{Z}_n$ is applied to minimize the local minima points, and the var is also used to ensure the minima points occur periodically. The overall functionals, $\mathbf{G_1}$, and $\mathbf{G_2}$ are minimized to find the zeros of the Bessel function and estimated motion parameter values that approach the true motion parameters. In Equations (3.3) and (3.4), we set the values of the coefficients to $\epsilon_1 = 0.11$, $\epsilon_2 = 2$, $\epsilon_3 = 1$, $\mu_1 = 3.5$, $\mu_2 = 1$, $\mu_3 = 100$, and $\mu_4 = 0.12$. These values of the coefficients were found to be suitable based on extensive numerical experiments.

By using the lsqnonlin MATLAB® command [24], the motion parameters are obtained for the parameter set in Table 3.2 and are shown in Table 3.4. As may be seen, the estimated motion amplitudes are within 10% absolute error of the true values, except for no. 2, where determining the location of the zero of the Bessel function was difficult in the autocorrelation function (Figure 3.3(b)) as well. In the proposed method, the estimated motion parameters should be precise enough to compensate for the effect of the motion in the entire frequency range. Since the initial phase angle of the platform motion may not impact the radar cross-section of the ocean surface [50], we exclude it from the motion parameter estimation process.

Table 3.4: Estimated motion parameters for the parameter set in Table 3.2

No.	**True values**		**Estimated values**	
	$\boldsymbol{a}$ **(m)**	$\boldsymbol{\omega}$ $(\frac{\mathbf{rad}}{\mathbf{s}})$	$\boldsymbol{a}$ **(m)**	$\boldsymbol{\omega}$ $(\frac{\mathbf{rad}}{\mathbf{s}})$
1	10	0.08	9.0005	0.0601
2	2	0.05	2.3121	0.0405
3	5.5	0.02	5.2688	0.0171
4	1.228	0.127	1.2275	0.1270

3.2.4 Motion Compensation

With the fourth set of estimated motion parameters in Table 3.4, motion compensation was performed in the time domain. Figure 3.5(a) shows the autocorrelation of the received signal from the fixed antenna and antenna on a floating platform for case (4) at SNR=10 dB. The motion-compensated autocorrelation is calculated by dividing the autocorrelation related to the floating antenna by the estimated motion factor $J_0(2z\sin(\omega_p t/2))$ which includes estimated motion parameters and is compared with the autocorrelation of the received signal from the fixed antenna in Figure 3.5(b).

Additionally, the Doppler spectrum for the fixed antenna and the antenna on a floating platform cases, and the motion-compensated spectrum are simulated using the estimated motion parameters. The aim of motion compensation is to retrieve the motion-free spectrum from the motion-contaminated spectrum with high accuracy. As shown in Figure 3.5(b), the retrieved autocorrelation function of the electric field coincides with the autocorrelation of the fixed antenna, except at two points (approximately at 19 and 31 s) which is the result of the small discrepancy between the true and estimated motion values. This shows that the choice of the initial guess and accuracy of the estimated parameters can significantly affect the recovered spectrum.

In Figures 3.6 and 3.7, the Doppler spectra for the fixed antenna and an antenna on a floating platform cases, and a motion-compensated Doppler spectrum are depicted, and the error between fixed and motion-compensated spectra is plotted in Figure 3.8. As can be seen from Figure 3.7(d), the motion-compensated spectrum matches closely with the spectrum received from the fixed antenna. Additionally, the motion-induced peaks are mostly removed from the motion-compensated spectrum, while the energy from the first- and second-order peaks is successfully recovered.

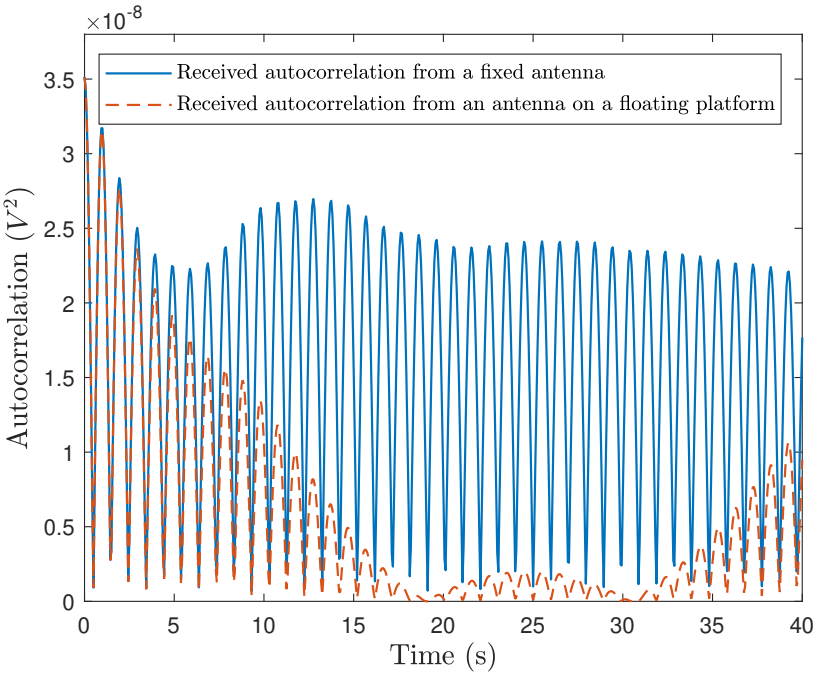

(a)

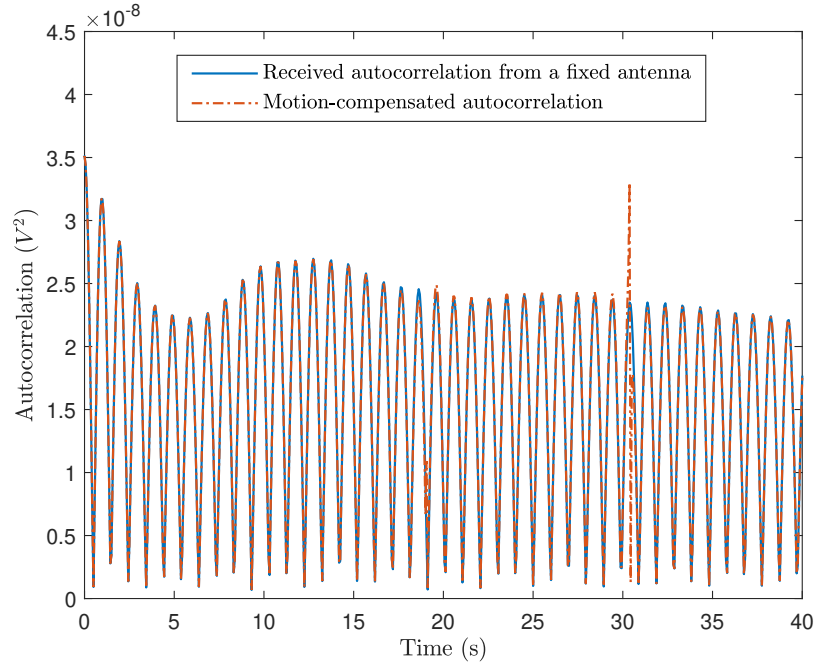

(b)

Figure 3.5: (a) Autocorrelation of the received signal of the fixed antenna and antenna on a floating platform, (b) autocorrelation of the fixed antenna, and time-domain motion-compensated autocorrelation. Motion parameters are assumed to be from set no. 4 in Table 3.2. The signal-to-noise ratio is taken to be 10 dB.

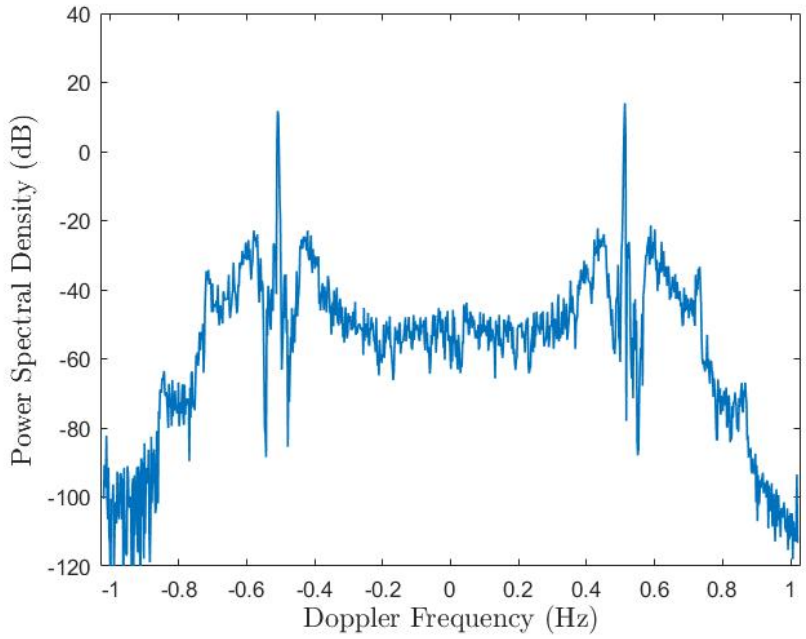

(a)

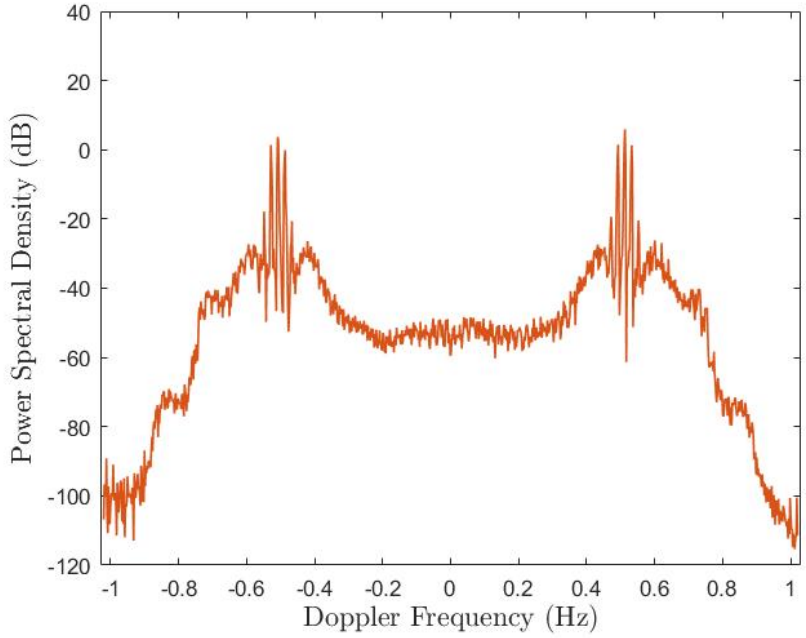

(b)

Figure 3.6: (a) Doppler spectrum of the fixed antenna, (b) antenna with motion. The signal-to-noise ratio is taken to be 10 dB.

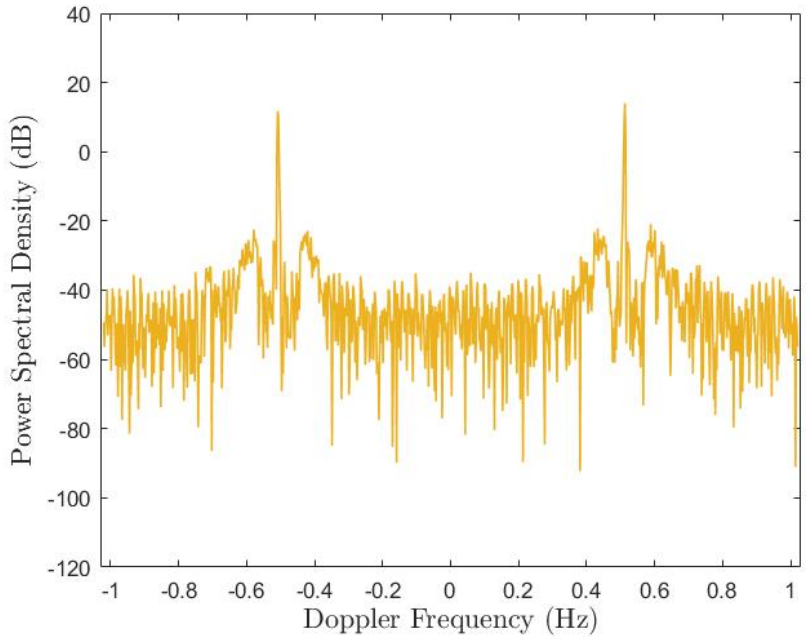

(a)

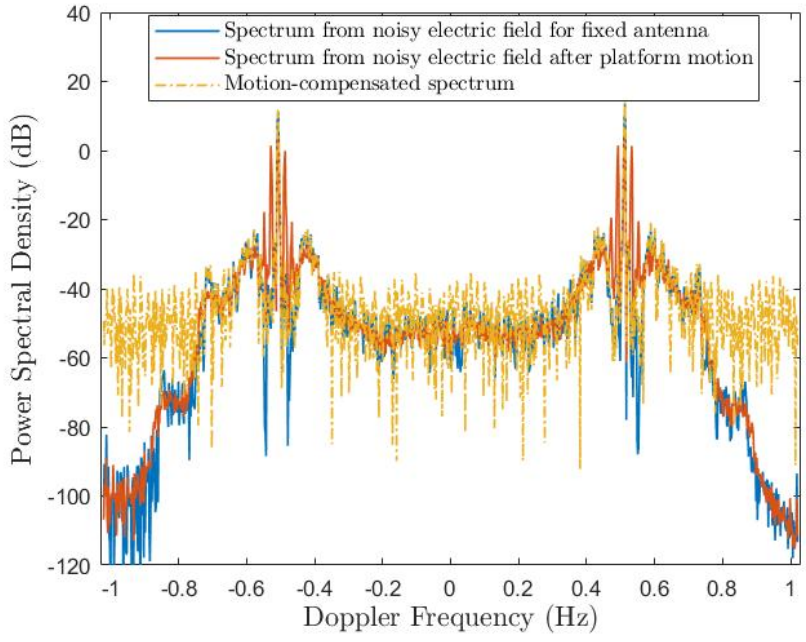

(b)

Figure 3.7: (a) Motion-compensated data from the antenna for the motion parameters no. 4 in Table 2. (b) Overlap of Figures 3.6(a), (b), and 3.7(a). The signal-to-noise ratio is taken to be 10 dB.

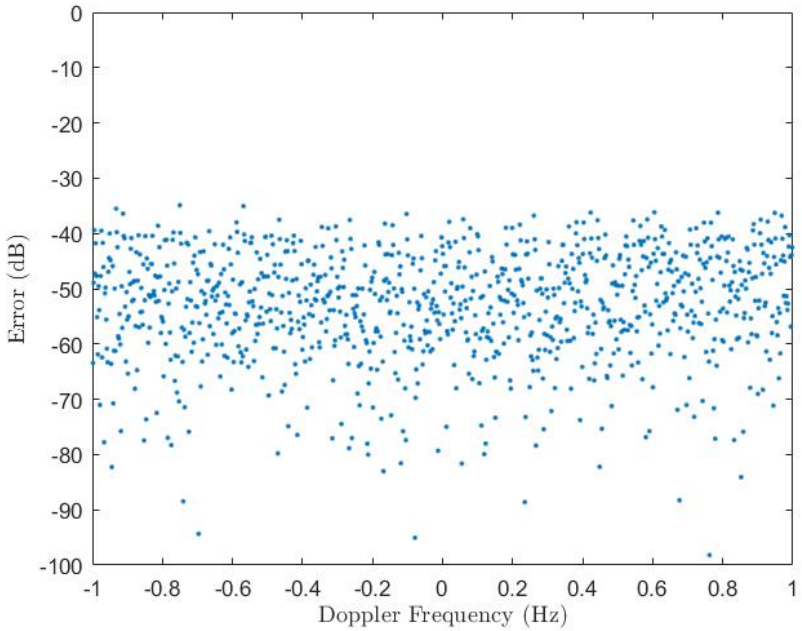

Figure 3.8: Error between the spectrum of the fixed antenna and motion compensated spectrum in dB vs. Doppler frequency.

In our solution to the motion parameter identification and motion compensation problems, there is a slight inconsistency between the actual and estimated motion parameters. Because in the frequency domain, the motion-contaminated Doppler spectrum has a series of peaks on each side of the main Bragg peak, if the motion parameters are not determined extremely precisely, then some of this peak energy remains in the Doppler spectrum. In this case, the side peak energy will not be eliminated entirely in the frequency domain, and this energy will lead to additional noise in the time domain and, thus, an increase in the noise floor.

Figure 3.9 compares the Doppler spectra obtained from motion parameters in the range of the actual and estimated values of the motion parameters. The noise floor decreases as the estimated motion parameter values used for motion compensation approach their true values. More investigation is needed to analyze this phenomenon comprehensively. Monte Carlo simulation is also performed for 100 iterations to show the error distribution. A normal distribution with a standard deviation of 10% of the mean with mean values of $a = 1.228$ (m) and $\omega = 0.127$ (rad/s) are considered as the true values. The mean and standard deviation of the results of the motion parameters estimation is shown in Table 3.5. The estimated standard deviation is larger than the

true standard deviation due to the limited sample size. In comparison to [4], motion

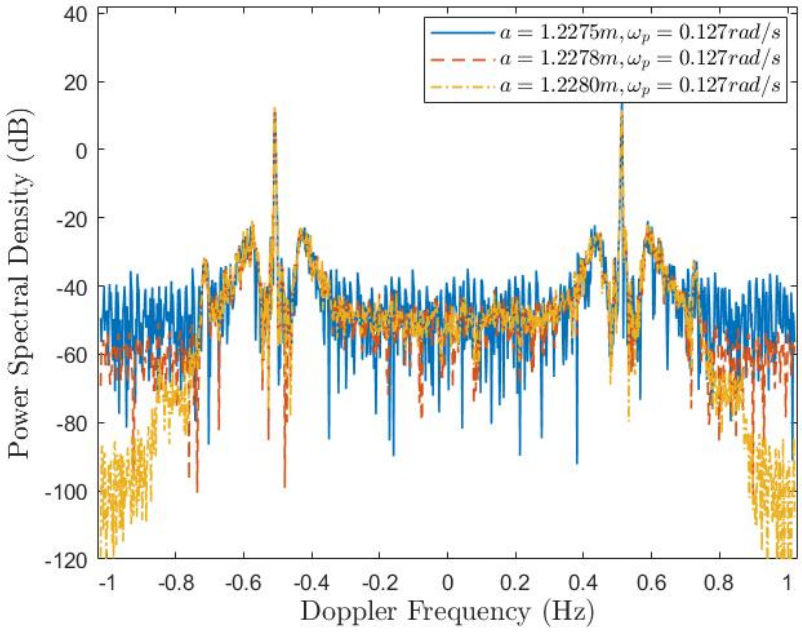

Figure 3.9: Comparison of various Doppler spectra obtained from motion parameter values close to estimated and actual values of the motion parameters.

compensation can be performed accurately with the proposed technique without *a priori* knowledge of the platform motion parameters.

Table 3.5: Error distribution calculated from Monte Carlo simulation for set 4 of the motion parameters in Table 3

Parameters	**True values**		**Estimated values**	
	$\boldsymbol{a}$ **(m)**	$\boldsymbol{\omega}$ $(\frac{\mathbf{rad}}{\mathbf{s}})$	$\boldsymbol{a}$ **(m)**	$\boldsymbol{\omega}$ $(\frac{\mathbf{rad}}{\mathbf{s}})$
Mean($\boldsymbol{\mu}$)	1.2286	0.1327	1.2475	0.1199
Standard Deviation($\boldsymbol{\sigma}$)	0.1263	0.0036	0.1942	0.0036

3.3 Method 2: Motion Parameter Estimation Based on Frequency Location and Amplitude of the Motion-Induced Peaks in Radar Doppler Spectrum

3.3.1 Proposed Solution

This technique uses the relationship between the frequency location and intensity of the motion-induced peaks and the frequency and amplitude of the platform motion to estimate the motion parameters. These values are next applied in the time-domain motion-compensation relation to recover the radar Doppler spectrum.

It was shown that the motion-induced peaks are located symmetrically at $\omega_d = \pm\omega_B \pm n\omega_p$ frequencies, with ω_B denoting the Doppler frequency of the Bragg peaks,

$$\omega_B = \sqrt{2gk_0}, \tag{3.5}$$

where $k_0 = 2\pi f/c$ and c is the speed of light in a vacuum [8]. Therefore, knowing the frequency locations of the motion-induced peaks in the Doppler spectrum, the radian frequencies of the platform motion can be determined through this linear relation once any frequency shifts due to underlying surface currents have been removed. Additionally, the amplitude of the platform motion can be estimated from the intensity of the motion-induced peaks through nonlinear Equations (3.6) and (3.7). Since the initial phase of the platform motions does not affect the RCS, it was excluded from the estimation process. Table 3.6 shows the Bragg and motion-induced peaks' frequency locations and relative amplitudes. The relative amplitude represents the ratio of the actual peak amplitude to the Bragg peak amplitude related to the fixed antenna. Parameter z can be obtained by Equation (2.15), and n is the order of the Bessel function.

$$|\sigma_{floating}(\pm\omega_B)| = |\sigma_{fixed}(\pm\omega_B)| \cdot J_0^2(z) \tag{3.6}$$

$$|\sigma_{floating}(\pm\omega_B \pm n\omega_p)| = |\sigma_{fixed}(\pm\omega_B)| \cdot J_n^2(z) \tag{3.7}$$

Table 3.6: The radian frequencies and relative amplitudes of Bragg peaks and motion-induced peaks.

Type of peaks	**Doppler frequency**	**Relative amplitude**
Bragg peaks	$\pm\omega_B$	$J_0^2(z)$
Motion-induced peaks	$\pm\omega_B \pm n\omega_p$	$J_n^2(z)$

From Equations (3.6) and (3.7), six nonlinear Equations can be obtained based on the relative amplitudes, in which four unknown parameters exist. Two of the unknowns are the motion parameters (a and ω_p), and the other two are the Bragg peak intensities related to the fixed antennas ($|\sigma_{fixed}(\pm\omega_B)|$). Among these six equations, the ones with the greater motion-induced peak intensities were chosen. By solving these nonlinear equations in an optimization process, using the lsqnonlin command in MATLAB® [24], motion parameters, including amplitudes and angular frequencies, can be estimated.

3.3.2 Simulation and Analysis

The first- and second-order RCSs for the fixed antenna case are calculated from Equations (2.4) to (2.12) and plotted in Figures 3.10(a) and (b). The total RCS, which is assumed to be equal to the sum of the first- and second-order RCSs (i.e., as is typical, orders of scatter beyond second-order are ignored), is shown in Figure 3.11. The set of parameters used for synthesizing the data is listed in Table 3.7.

In the next step, by using Equations (2.17) and (2.18), the received electric field and its autocorrelation function are obtained. The autocorrelation of the received signal of the antenna on a floating platform is calculated by multiplying the autocorrelation of the received signal of the fixed antenna by the motion factor $J_0(2z\sin(\omega_p t/2))$. Since the RCS for an assumed patch is proportional to the Fourier transform of the autocorrelation function (power spectral density spectrum), instead of using the RCS in Equations (3.6) and (3.7), amplitudes of the Bragg peaks and motion-induced peaks in power spectral density spectrum were applied.

The initial guesses are taken to be $a = 1.220$ m, and $\omega = 0.120\ \frac{rad}{s}$, and the Bragg peak intensities are assumed to be 5 dB. In the first step, the initial values are chosen randomly, and after several simulations and investigations, these values are selected

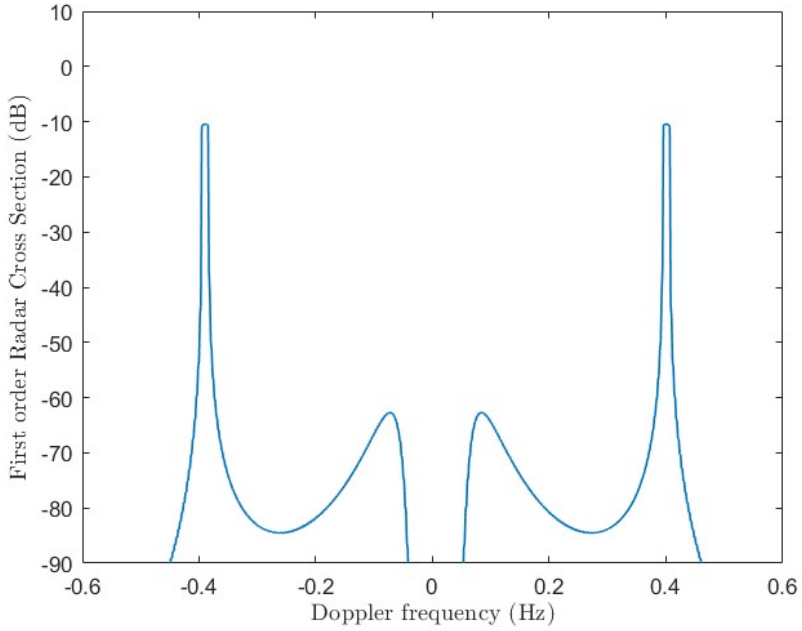

(a)

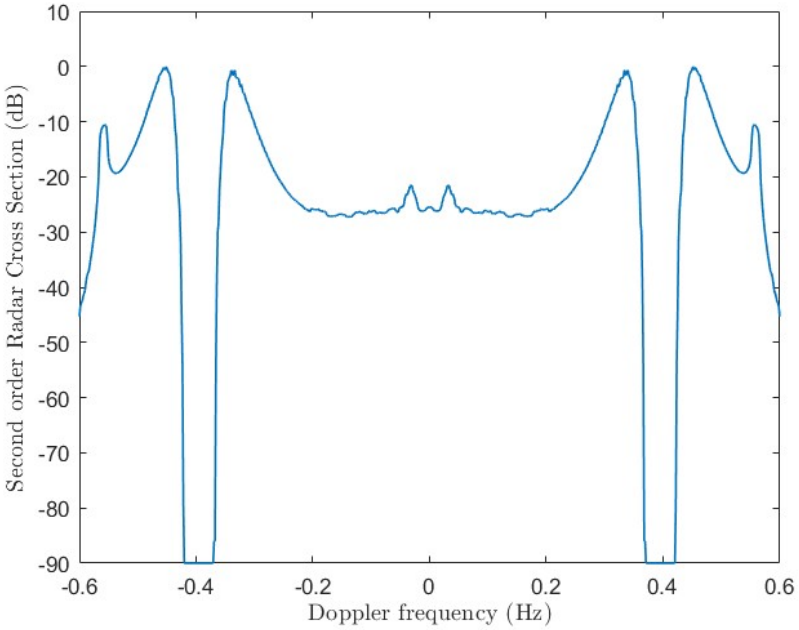

(b)

Figure 3.10: (a) First-order and (b) second-order radar cross-section of ocean surface for the fixed antenna case.

Table 3.7: Parameter set considered in the simulation [47]

Wind speed	20 knots
Antenna transmission frequency	15 MHz
Patch width	2500 m
Significant wave height	2.06m
Peak power	16 kW
Half power beamwidth	0.07029 rad
Transmitter gain	1.585
Receiver gain	65.76
Distance from the path to transmitter	50 km
Distance from the path to receiver	50 km

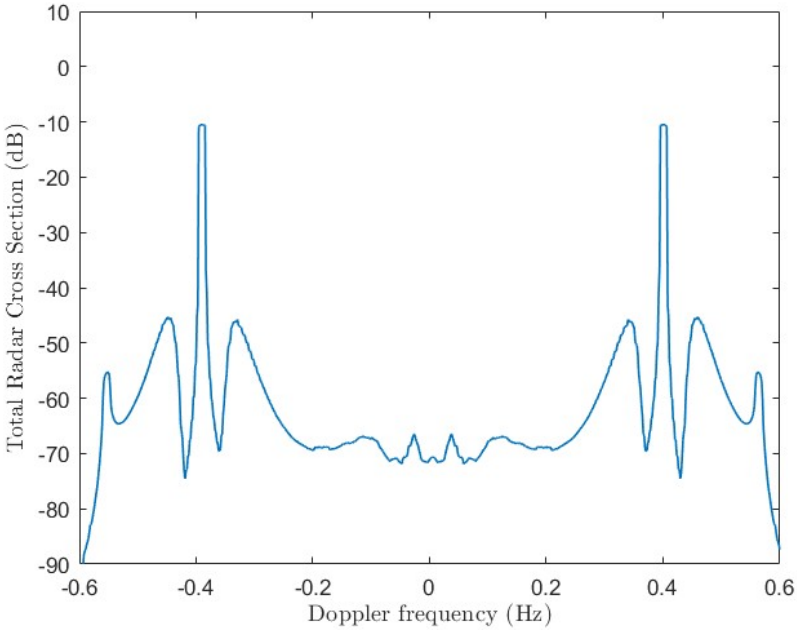

Figure 3.11: Total radar cross-section, which is the sum of first- and second-order radar cross-sections, for the fixed antenna case.

to give the best result. The phase shifts for both frequencies are taken to be 0.02 radians. The signal-to-noise ratio is taken to be 30 dB. Also, the order of the Bessel function, n, is taken to be 1. A moving average window was applied to smooth the RCSs; otherwise, the motion parameters cannot be found precisely because of the intrinsic oscillatory nature of the Doppler spectrum.

The estimated parameters can be found in Table 3.8. The Doppler spectra for the fixed antenna and the antenna on a floating platform cases, and the motion-compensated spectrum are shown in Figures 3.12 and 3.13(a). Also, the error between the power spectral density for the fixed antenna case and motion-compensated power spectral density is shown in Figure 3.13(b). Figure 3.14 shows the overlap of Figures 3.12 and 3.13(a) for comparison. In Figure 3.14, blue (solid) lines are associated with the Doppler spectrum for the fixed antenna case, red (dashed) lines correspond to the antenna on a floating platform case, and yellow (dash-dotted) lines are the motion-compensated spectrum. This figure shows that the effect of the motion is compensated for and motion peaks are removed, and the energy of the Bragg peaks is also recovered. The root-mean-square error (RMSE) between the motion-compensated and fixed antenna spectra was found to be 0.0022.

Table 3.8: True values and results of the simulation

Motion parameters	**True values**	**Results**
a **(m)**	1.228	1.190
ω **(rad/s)**	0.127	0.126

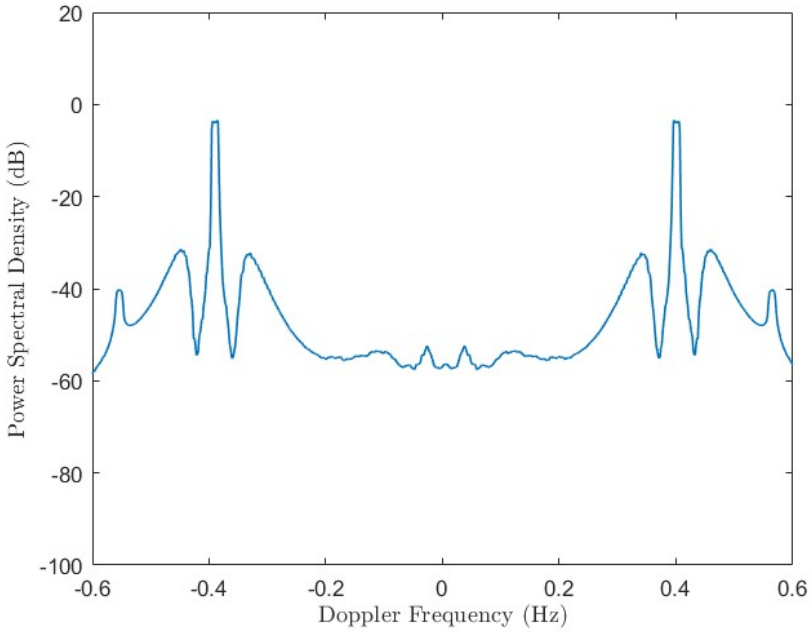

(a)

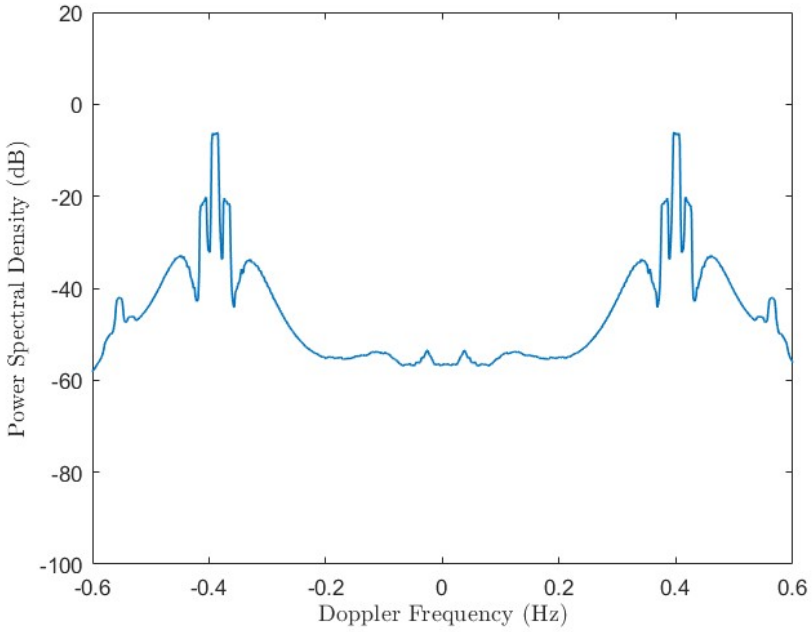

(b)

Figure 3.12: a) Doppler spectrum of the fixed antenna, b) Doppler spectrum of the antenna on a floating platform.

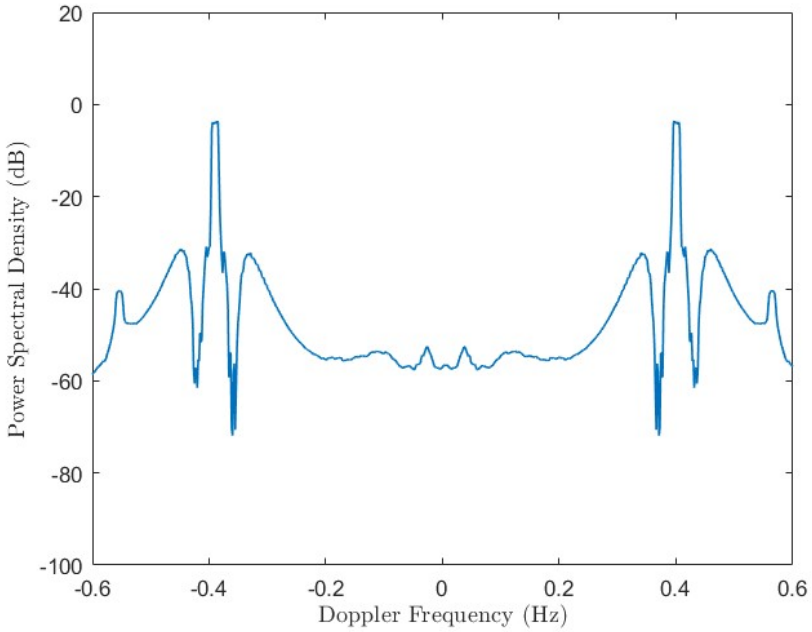

(a)

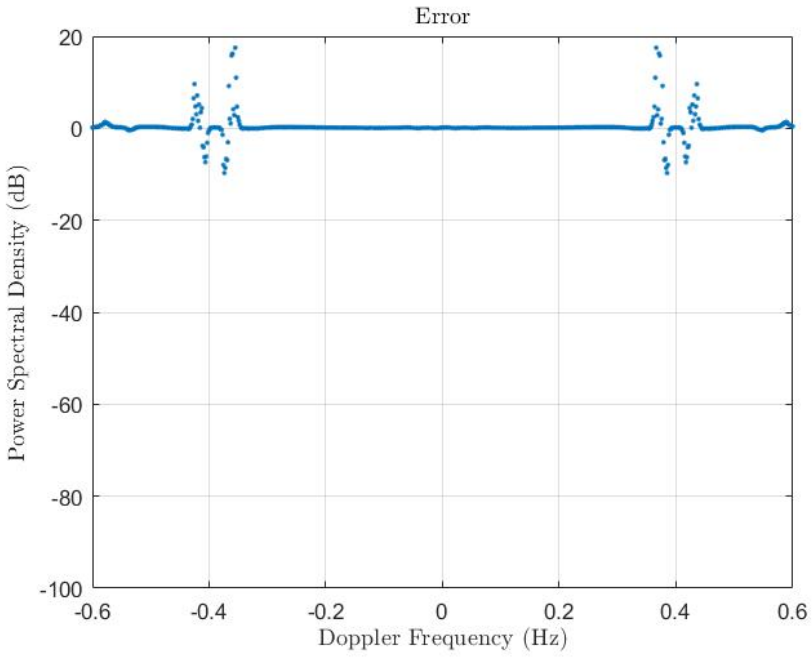

(b)

Figure 3.13: a) Motion compensated spectrum, b) Error between the fixed case and the motion-compensated spectrum.

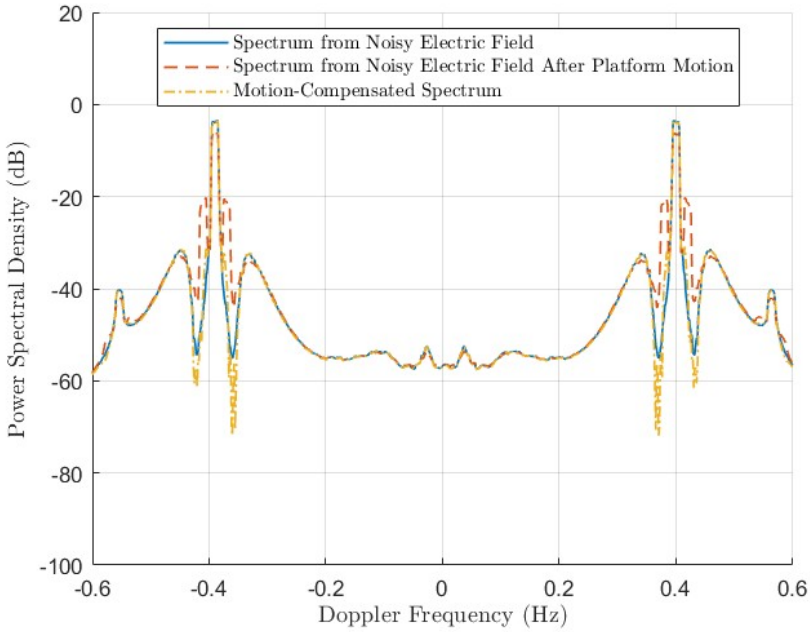

Figure 3.14: Overlap of Figures 3.12 and 3.13(a) for comparison.

It is important to highlight that in this thesis, the SNR has been defined as the ratio between the signal and noise power. In addition, the external white noise is modulated by the platform's motion due to the limited system bandwidth. Although the proposed methods consider different SNR values, it's worth noting that the noise floor in the first motion compensation method (Figure 3.7a) is -50 dB. Consequently, any Doppler spectra information below -50 dB is subject to contamination and interference from external white noise. The second method focuses on a narrower spectral range, encompassing frequencies slightly below and the $\pm\sqrt{2}\omega_B$ peaks at both ends of the spectrum. This specific range is of particular interest for extracting ocean wave spectra and estimating wave heights. Additionally, by applying smoothing techniques to the calculated RCSs, the second method appears to introduce less noise into the ocean wave spectrum, which is a significant advantage over the first method.

3.4 Chapter Summary

In this chapter, two methods for motion-parameter (amplitude and angular frequency) identification for an antenna on a floating platform were presented, and motion compensation was performed in the time domain using the estimated parameters. First, the radar cross-section of the ocean surface for a fixed antenna case and the received electric field were simulated. In order to analyze the effect of the platform motion in the time domain, the radar cross-section of the ocean surface for the case of an antenna on a floating platform can be expressed as the product of the radar cross-section for a fixed antenna case and a zeroth-order Bessel function of the first kind. In the first method, the autocorrelation function of the received electric field was used to obtain the motion parameters. To do so, the autocorrelation of the received electric field for a fixed antenna and an antenna in motion were compared, and based on the location of the zeros of the zeroth-order Bessel function of the first kind, motion parameters were estimated. In addition, it was shown that the frequencies and relative intensities of the motion-induced peaks were functions of the motion parameters. The second method used the locations and intensities of the Bragg peaks and motion-induced peaks to calculate the motion parameters. The recovered Doppler spectrum was obtained from the motion-contaminated Doppler spectrum using these estimated motion parameters and coincided closely with the motion-free spectrum.

Chapter 4

Significant Wave Height Estimation from the Signal Received from an Antenna on a Floating Platform

4.1 Introduction

This chapter proposes a technique for significant wave height estimation from up to second-order backscatter when the transmitter is mounted on a floating platform. The sinusoidal platform motion model is assumed to include a single frequency in a single direction. The significant wave height is estimated from the variance of the upper envelope of the received electric field. While, using previous methods, the significant wave height would be calculated from the motion-compensated Doppler spectrum of the antenna, neither motion compensation nor prior motion parameter knowledge is necessary using the method proposed in this chapter. However, the proposed method does require a calibration stage that can be implemented using the data collected by a wave buoy or by analyzing the data using the adapted Barrick method.

Section 4.2 describes the basic theory and methodology of the proposed significant wave height estimation technique. The results of the simulation and analysis are presented in Section 4.3. A summary of the chapter is provided in Section 4.4.

4.2 Method

By restricting attention to a monostatic configuration and referring to Figure 4.1, it was shown in [37] that the first-order normal component of the received electric field (including the second-order hydrodynamic scatter) could be determined by

$$(E_{0_n}^{+})_1(\omega) \approx -\frac{j\omega C_0}{(2\pi)^2}\int_{\tau}\frac{F^2(r)}{r}\int_{\theta}\frac{\partial\xi(x_1,y_1,t)}{\partial r}d\theta e^{-j\omega\tau}d\tau \tag{4.1}$$

where C_0 is a constant including the antenna parameters, F denotes the Sommerfeld attenuation function, τ is the two-way electrical field travel time, which is $\tau = 2r/c$, and r and c are the distance between the transmitter and receiver to the scattering patch, and the speed of light in a vacuum, respectively. The variable ξ denotes the vertical ocean surface displacement.

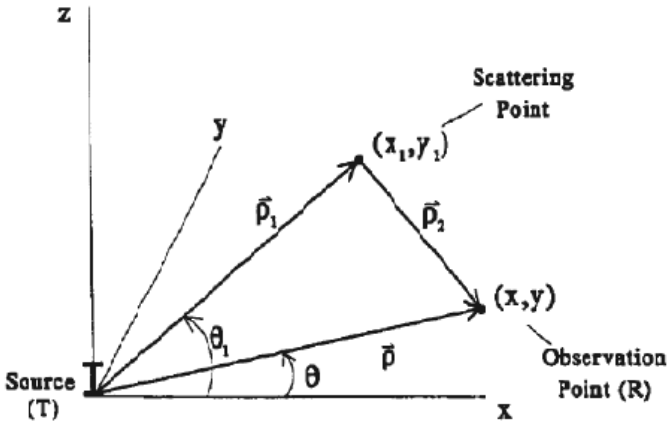

Figure 4.1: General first-order bistatic scatter geometry with stationary antennas [51].

By using the definition of the continuous-time Fourier Transform and Divergence Theorem and considering that, along the scattering circle, r and τ are constant,

$$(E_{0_n}^{+})_1(\tau) \approx \mathcal{F}_{\tau}^{-1}\left[-\frac{j\omega C_0}{(2\pi)^2}\right] * \int_{\theta}\frac{F^2(r)}{r}\frac{\partial\xi(x_1,y_1,t)}{\partial r}d\theta \tag{4.2}$$

$$(E_{0_n}^{+})_1(t) \approx M_1\frac{F^2(r)}{r}\int_{x_1}\int_{y_1}\Delta\xi(x_1,y_1,t)dy_1dx_1 \tag{4.3}$$

where M_1 is a constant. By using the fact that waves with a wavenumber of $2k_0$ are

the primary source of first-order energy [51], $\Delta\xi \approx 4k_0^2\xi$ and

$$(E_{0_n}^+)_1(t) \approx M_2 \int_{x_1} \int_{y_1} \xi(x_1, y_1, t) dy_1 dx_1, \tag{4.4}$$

$$M_2 = \frac{4k_0^2 F^2(r)}{\tau} M_1 \tag{4.5}$$

Therefore, for a single scattering ocean patch,

$$(E_{0_n}^+)_1(x_1, y_1, t) \approx M_2 \xi(x_1, y_1, t) \tag{4.6}$$

Considering that $H_s = 4\sigma_\xi$, where σ_ξ is the standard deviation of the ocean surface displacement, and by taking the standard deviation of both sides of Equation (4.6)

$$\sigma_{(E_{0_n}^+)_1} \approx AH_s + B \tag{4.7}$$

where A and B are constants, and B denotes received noise power. Also, it was found in [38] that the second-order scattered electric field, which includes the hydrodynamic and electromagnetic scatters, is proportional to the square of the ocean surface displacement minus 1 ($\xi^2 - 1$). It can thus be concluded that up to the second-order,

$$(E_{0_n}^+)(t) \approx A'\xi^2 - A' + B'\xi + C' \tag{4.8}$$

where A', B' and C' are constants, and C' corresponds to the power of the received noise. By taking the upper envelope and the variance of both sides of Equation (4.8), the following equation was obtained [38]:

$$\mathrm{Var}[E_{UpperEnvelope}(t)] \approx \frac{16A'^2}{H_s^2} + B'^2 H_s^2 \frac{4-\pi}{32} + C' + 2A'B' \left(3\frac{\sqrt{\pi}}{4}\frac{H_s^{3/2}}{8} - \sqrt{\frac{\pi}{2}} - \frac{\sqrt{2\pi}H_s}{4} \right) \tag{4.9}$$

To employ this equation, the upper envelope of each side of Equation (4.8) is taken. The upper envelope of ξ is known to follow a Rayleigh distribution [52]. Var denotes the variance, and $E_{UpperEnvelope}$ is the upper envelope of the received electric field. In deriving Equation (4.9), the fact that if the random variable X follows a Rayleigh distribution, then X^2 follows an exponential distribution and the definition of H_s, where it is given to be equal to four times the standard deviation of ξ, were used. It should be noted that before being able to estimate H_s reliably, the proposed methods

require a calibration step to determine the constants A', B', and C'.

First- and second-order RCSs of the ocean surface for a fixed monostatic radar system are simulated in MATLAB® [24] using Equations 2.1 to 2.12, and the electric field is obtained from the total RCS through 2.15 and 2.16. The transmitter antenna is assumed to be deployed on a floating platform, and the receiver antenna is taken to be stationary. For a basic demonstration of the proposed method, the platform motion model is assumed to consist of a single frequency of motion in a single direction [3]. The time-varying value of $\delta\vec{\rho_0}$, the platform displacement, is given by the expression

$$\delta\vec{\rho_0}(t) = [a\cos(\omega_p t + \phi)]\hat{\rho}_p \tag{4.10}$$

where a, ω_p, and ϕ are the amplitude, radian frequency, and the initial phase of the cosine function, respectively, t is time, and the direction of the platform motion is indicated by $\hat{\rho}_p$.

The received electric field from a transmitter on a floating platform [4] can be calculated by modulating the received electric field from a fixed transmitter by a complex exponential factor containing the platform motion parameters according to

$$E_{\text{floating}}(t) = E_{\text{fixed}}(t) \cdot e^{jz\cos(\omega_p t)} \tag{4.11}$$

$$z = 2ak_0\cos(\theta_k - \theta_p) \tag{4.12}$$

E_{floating} and E_{fixed} are the received electric fields for the case of an antenna on a floating platform, and the fixed-antenna case, respectively. θ_k represents the direction of the ocean wave vector, and θ_p denotes the platform direction of motion in x-y plane.

It is important to mention that in the spectrum simulations conducted in this thesis, we utilized the Pierson-Moskowitz spectrum. This spectrum is defined based on the wind speed, and does not incorporate the significant wave height as an input parameter. Therefore, we converted the significant wave height to wind speed using the following equation [53].

$$U = \sqrt{\frac{gH_s}{0.21}} \tag{4.13}$$

The variance and next mean of the variance of the antenna's electric field on the floating platform are calculated for each synthesized data set. For calibration, the

coefficients A', B', and C' can be calculated in MATLAB® [24] using H_s' which is the significant wave height previously measured by a buoy during a prior calibration phase. If a buoy is deployed for some period during which the radar data is being collected, we can use the wave buoy data to estimate the proportionality coefficients A', B', and C'. There is no time dependence for these three coefficients, and their dependence on the patch location is known. This known spatial dependence makes this calibration method applicable to determine H_s for any other ocean patch at any other time [38]. To perform the calibration, buoy data is assumed to have uniform distribution with 25% absolute error, and the coefficients are found using nonlinear data-fitting in the least-squares sense.

The other option for calibration is to calculate H_s' from the motion-compensated spectrum of the radar on a floating platform by Barrick's method [27]. Barrick showed that the significant wave height could be estimated from the expression

$$H_s^2 = 4\frac{\int_{-\infty}^{+\infty} \sigma_{(2)}(\omega_d)/W(\omega_d/\omega_B)d\omega_d}{k_0^2 \int_{-\infty}^{+\infty} \sigma_{(1)}(\omega_d)d\omega_d} \tag{4.14}$$

where $\sigma_{(1)}$ and $\sigma_{(2)}$ are the first- and second-order RCSs, respectively. ω_d is the Doppler frequency and the weighting function $W(.)$ is determined by averaging the coupling coefficient over all frequencies. The influence of the wave period and direction are disregarded in this empirical method. In this chapter, the scaled version of (4.14) has been used [29, 37]. The scaling factor ξ_s was specified as [37]

$$\xi_s = \begin{cases} 0.55 & H_s \leq \frac{2}{3k_0} \\ \min\left(1, 0.55 + \frac{1}{2}\left(H_s - \frac{2}{3k_0})\right)\right) & H_s > \frac{2}{3k_0} \end{cases} \tag{4.15}$$

where, for the operating frequency of 15 MHz, when $H_s \leq 2.12$ (m) scaling factor is 0.55, and otherwise, the estimated H_s is scaled by $\min\left(1, 0.55 + \frac{1}{2}\left(H_s - \frac{2}{3k_0})\right)\right)$.

The motion compensation can be performed by the technique discussed in [54], which does not require prior knowledge of the motion parameters. That method which was discussed in Chapter 3 (Section 3.2), estimates the motion parameters from the autocorrelation of the received electric field. Although a motion-compensated spectrum will be used in that case for calibration, it is not required after it has been applied in the calibration step. Motion-contaminated spectra cannot be used for accurate H_s

estimation with the Barrick method referred to here since the spectrum of the antenna on a floating platform will be contaminated by some motion-induced peaks. These peaks make the estimation of significant wave height highly inaccurate, resulting from incorrect Bragg peak energy calculation. This phenomenon adversely affects the extraction of ocean surface parameters, such as wind speed, the non-directional wave spectrum, and significant wave height.

After finding the least-square estimate of coefficients A', B', and C' from the significant wave height measured from the buoy or the motion-compensated spectrum of the antenna on a floating platform, these constants are used to provide an estimated value for H_s by solving Equation (4.9).

4.3 Simulation and Analysis

The proposed method was applied to synthetic data due to the lack of available measured field data from an HF radar on a floating platform. The received electric field from an antenna on a floating platform is simulated by considering the motion parameters $a = 1.228$ m, $\omega_p = 0.227$ rad/s, and motion direction of 0.02 rad. The parameter set which was used in the simulation process is according to Table 3.3.

Simulations are conducted to assess the method's performance at different radar frequencies and sampling periods for low, moderate, and high sea states. Both Equations (4.7) with which H_s can be calculated from the first-order received electric field (including the second-order hydrodynamic scatter), and 4.9 with which H_s can be calculated from up to the second-order received electric field (including hydrodynamic and electromagnetic scatters), are used to determine H_s and analyze the effect of considering the second order returns in the equation. Results of simulations with the assumption that H_s' was obtained from a deployed wave buoy are plotted in Figures 4.2 and 4.3 for the first-order method and Figures 4.4 and 4.5 for up to the second-order method. Figures 4.2 and 4.4 shows the estimated H_s for various sampling periods ($T_s = 0.1, 0.4$, and 0.6 s). The operating frequency is taken to be 15 MHz. The estimated H_s versus the true values of H_s are also shown for different operating frequencies of f= 5, 10, and 20 MHz in Figure 4.3 and 4.5. The signal-to-noise ratio of the received electric field is taken to be 10 dB for all of the simulations in this study. The RMSE for each of these cases has also been calculated.

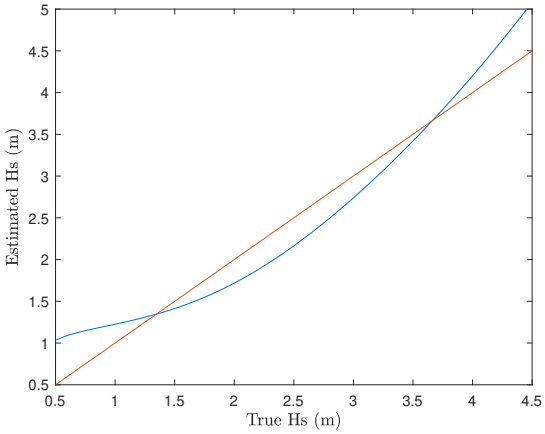

(a)

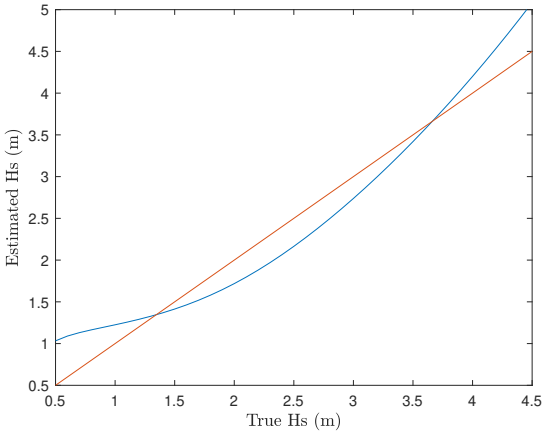

(b)

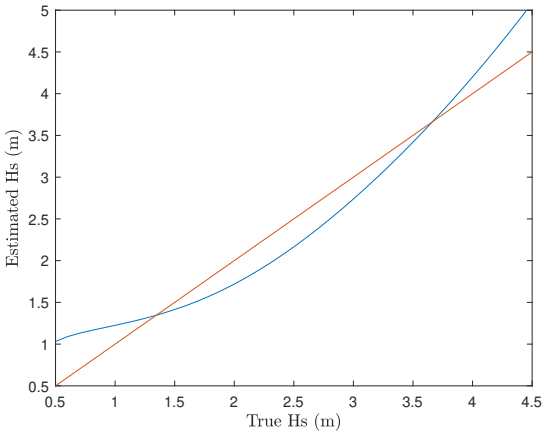

(c)

Figure 4.2: Estimated versus true values of significant wave height obtained from the first-order received field from a radar with a fixed operating frequency of 15 MHz and different sampling periods. (a) T_s= 0.1 s, (b) T_s = 0.4 s, (c) T_s= 0.6 s.

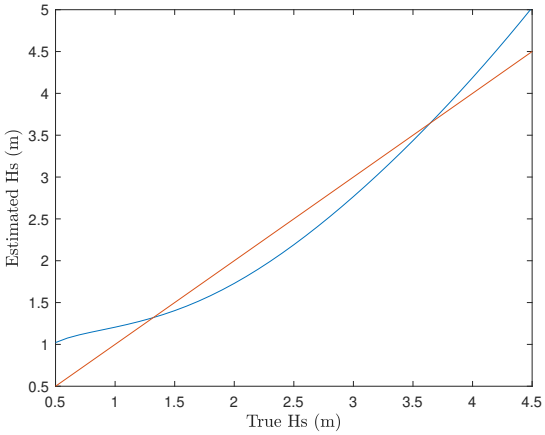

(a)

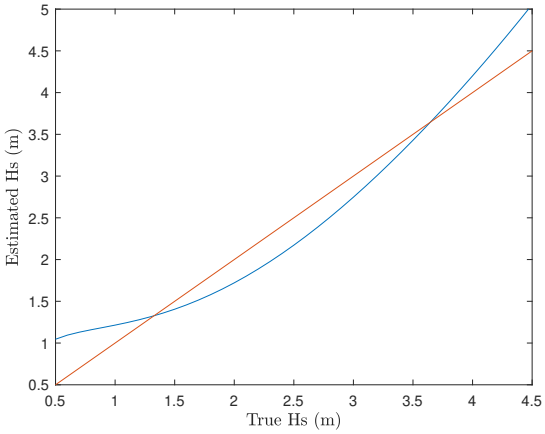

(b)

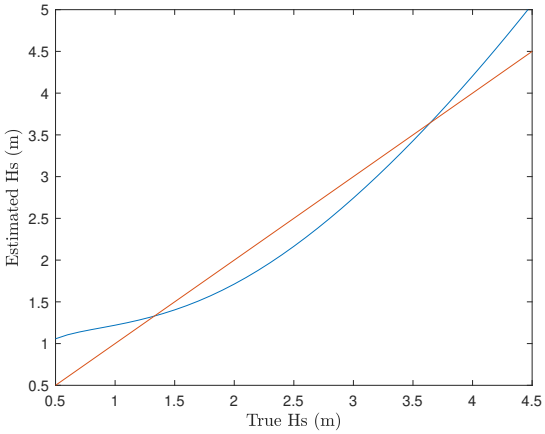

(c)

Figure 4.3: Estimated versus true values of significant wave height obtained from the first-order received field from a radar with the fixed sampling period of 0.4 s and different operating frequencies. (a) $f = 5$ MHz, (b) $f = 10$ MHz, (c) $f = 20$ MHz.

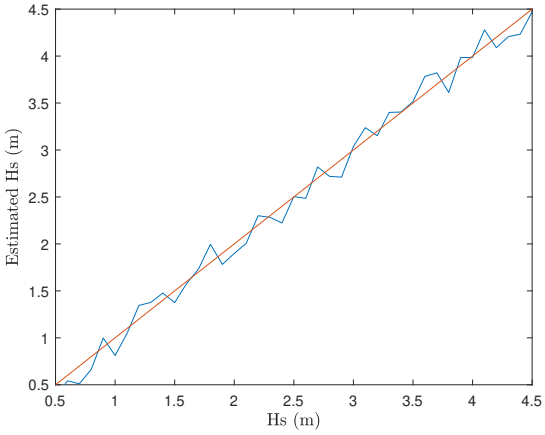

(a)

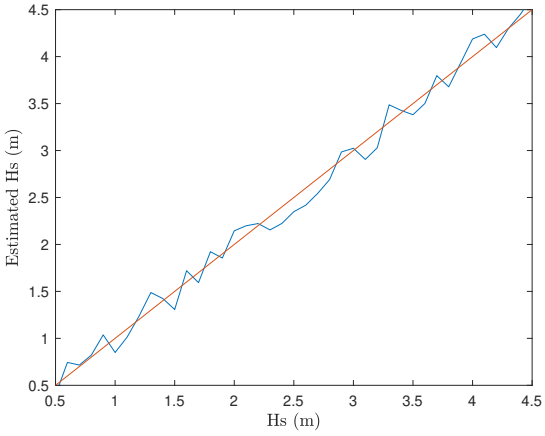

(b)

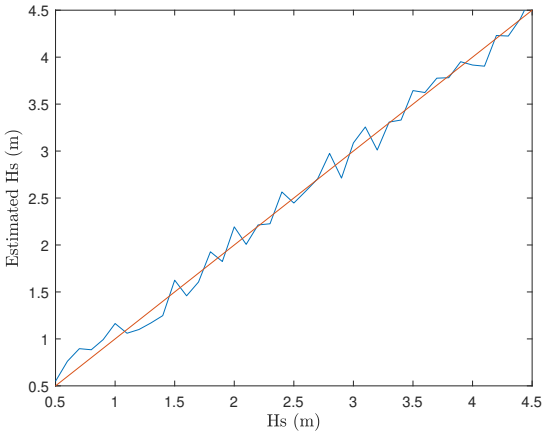

(c)

Figure 4.4: Estimated versus true values of significant wave height obtained from up to second-order received field from a radar with a fixed operating frequency of 15 MHz and different sampling periods. (a) T_s= 0.1 s, (b) T_s = 0.4 s, (c) T_s= 0.6 s.

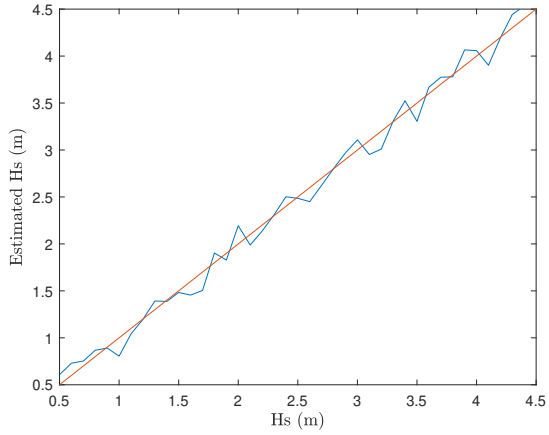

(a)

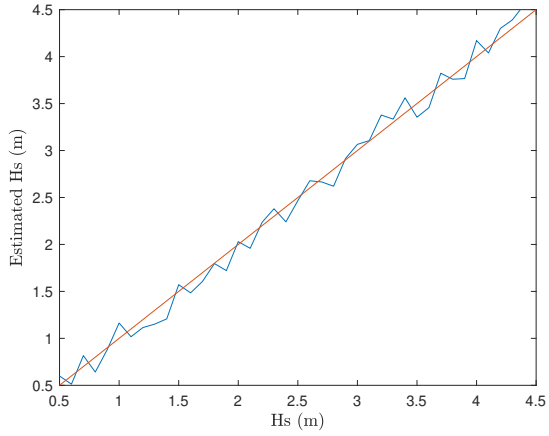

(b)

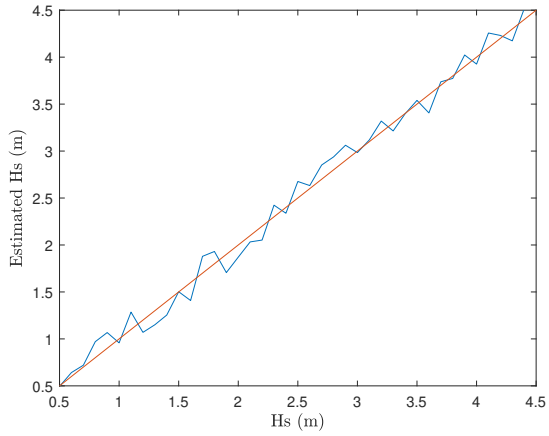

(c)

Figure 4.5: Estimated versus true values of significant wave height obtained from up to second-order received field from a radar with the fixed sampling period of 0.4 s and different operating frequencies. (a) $f = 5$ MHz, (b) $f = 10$ MHz, (c) $f = 20$ MHz.

Figure 4.6 shows the simulation results using H_s' values extracted by the adapted Barrick method [29, 37] from the Doppler spectrum with motion compensation applied with the technique from [54], from a transmitter on a floating platform. The radar's sampling period and operating frequency are taken to be 0.4 s and 15 MHz, respectively. Tables 4.1 and 4.2 show the results of the proposed method. The sets of coefficients A, B, A', B', and C' obtained from the simulation and the RMSE are summarized. From the figures and tables, it is clear that considering the second-order received electric field considerably affects the accuracy of the H_s estimation. In the worst case, by using 4.9, the correlation coefficient (CC) between the estimated H_s and true H_s values is 0.9947.

Table 4.1: Results from the proposed method (by applying first-order received electric field)

Figure No.	f **(MHz)**	T_s **(s)**	A	B	**RMSE (cm)**
4.2(a)	15	0.1	0.27×10^{-3}	0.38×10^{-3}	28.87
4.2(b)	15	0.4	0.13×10^{-3}	0.18×10^{-3}	29.84
4.2(c)	15	0.6	0.10×10^{-3}	0.15×10^{-3}	28.84
4.3(a)	5	0.4	0.14×10^{-3}	0.12×10^{-3}	28.88
4.3(b)	10	0.4	0.39×10^{-3}	0.49×10^{-3}	26.90
4.3(c)	20	0.4	0.47×10^{-3}	0.49×10^{-3}	28.29

Table 4.2: Results from the proposed method (by applying up to second-order received electric field)

Figure No.	f **(MHz)**	T_s **(s)**	A'	B'	C'	**RMSE (cm)**	**CC**
4.4(a)	15	0.1	0.0359×10^{-3}	0.3213×10^{-3}	0.0000×10^{-3}	11.74	0.9958
4.4(b)	15	0.4	0.0332×10^{-3}	0.3026×10^{-3}	0.0439×10^{-3}	12.29	0.9947
4.4(c)	15	0.6	0.0003	0.0028	0.0000	11.68	0.9952
4.5(a)	5	0.4	0.0004	0.0039	0.0000	11.10	0.9957
4.5(b)	10	0.4	0.0005	0.0050	0.0000	11.34	0.9960
4.5(c)	20	0.4	0.0003	0.0028	0.0000	11.93	0.9951
4.6	15	0.4	0.0232×10^{-3}	0.2515×10^{-3}	0.0000×10^{-3}	10.87	0.9960

Table 4.3: Results from analysis of required range of values of H_s' for accurate estimation of H_s (T_s= 0.4 s and f= 15 MHz)

Range of H_s' values (m)	A'	B'	C'	**RMSE (cm)**
0.5-1.5	0.0219×10^{-3}	0.7891×10^{-3}	0.0000×10^{-3}	13.33

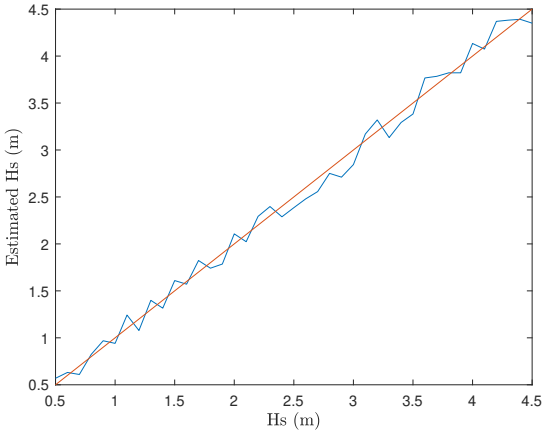

Figure 4.6: Estimated versus true values of significant wave height obtained by employing the H_s' extracted from motion-compensated spectrum in the calibration step.

In this chapter, we utilize the adapted Barrick method with appropriately compensated motion-contaminated Doppler spectrum as the initial estimate, demonstrating similar results to the calibration using buoy data. However, if the adapted Barrick method were directly employed for significant wave height extraction, it would lead to an increased RMSE of 53.18 cm. The comparison between the proposed method and the adapted Barrick method is illustrated in Figure 4.7. Notably, our proposed method enhances the accuracy of H_s estimation without necessitating motion compensation or prior knowledge of motion parameters, thereby highlighting its superior efficiency.

An analysis was performed to determine the range of H_s' required to accurately estimate H_s between 0.5 to 4.5 m. Table 4.3 shows the results of this investigation. If the wave buoy collects data for H_s values in the range of 0.5 to 1.5 m (depending on factors such as wind speed and fetch, it may happen over the course of several hours), the value of H_s may be estimated with an RMSE of 13.33 cm.

As seen from the Figures, the proposed method can properly estimate the significant wave height for H_s values between 0.5 and 4.5 m. Nevertheless, determining the coefficients requires variability of the received electric field over time. However, once the coefficients are calculated, this method can be used for the same patch at any other time.

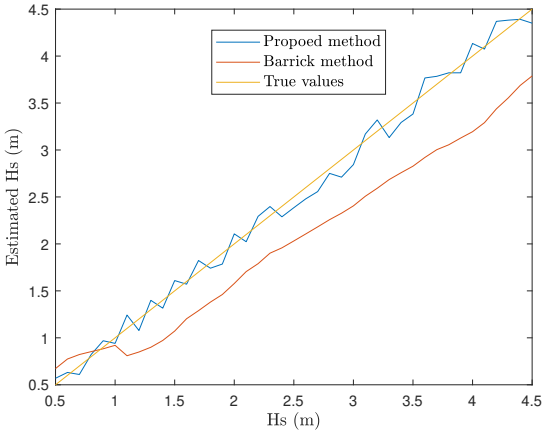

Figure 4.7: Comparison between the cases when the result of the adapted Barrick method is used as H_s' and when the adapted Barrick method is used directly for H_s estimation.

4.4 Chapter Summary

When the radar is mounted on a floating platform, significant ocean wave height estimation from the received electric field is investigated. The First-order received electric field is directly proportional to the ocean surface displacement. So, significant wave height can be determined from the linear relation between the standard deviation of the first-order received electric field and significant wave height. Considering up to the second-order received electric field, it was shown that the received electric field follows a quadratic relation with ocean surface displacement. Therefore, significant wave height is estimated from the relation between windowed variance of the upper envelope of the received electric field and significant wave height. A calibration stage is required to determine the significant wave height. This was done by employing a wave buoy and by using the significant wave height extracted from the Barrick method from the motion-compensated spectrum.

Simulations were conducted for various operating frequencies and, sampling periods for different sea states, and for both first-order and up-to second-order backscatter in significant wave height estimation. Results show that considering the second-order backscatter in addition to the first-order backscatter improves the estimated significant wave height value, with estimates having an RMSE of approximately 11 cm. Through the proposed approach, significant wave height can be estimated from the

received signal of the antenna on a floating platform without requiring knowledge of the motion parameters or motion compensation.

Chapter 5

Conclusion and Future Work

5.1 Conclusion

In this thesis, the aim was 1) to compensate for the effect of motion on the received signal from the antenna on a floating platform when the platform motion parameters (amplitude and frequency of motion) are not known *a priori*, and 2) to propose a method for significant wave height estimation from the received signal of the floating antenna in the time domain. The platform displacement is assumed to follow a single-frequency sinusoidal model in a single direction. The proposed techniques are based on a monostatic configuration by assuming a floating transmitter and fixed receiver.

In the first stage, the motion parameters of an antenna on a floating platform are identified, and motion compensation is performed in the time domain. Two motion parameter estimation methods are presented. In this regard, the first- and second-order radar cross-sections of the ocean surface for the case of a fixed antenna are simulated. The electric field and its autocorrelation have been calculated and converted to their floating counterpart. It was demonstrated in [5] that the radar cross-section of the ocean surface for the case of an antenna on a floating platform could be obtained by the product of the radar cross-section for the fixed antenna case and a motion factor. In the single-frequency platform motion model, the motion factor is a zeroth-order Bessel function of the first kind, and its argument contains the motion parameters. In the first method, the autocorrelation of the received electric field for a fixed antenna and an antenna in motion are compared, and based on the location of the zeros of the

zeroth-order Bessel function of the first kind, motion parameters are obtained. It was shown that when the amplitude of the motion in lower frequencies is high enough, this method can estimate the motion parameters with an absolute error of 10%. In addition, an error distribution is also obtained by Monte Carlo simulation.

In the second method, motion parameters are obtained based on the relationship between motion parameters, frequency location, and amplitude of the motion-induced peaks. Through this approach, the RMSE spectral error is 0.0022. The recovered Doppler spectrum is obtained from the motion-contaminated Doppler spectrum using these estimated motion parameters and coincides closely with the motion-free spectrum. The motion-compensated spectrum is free of motion-induced peaks, and the energies of first- and second-order peaks are successfully retained.

In the second stage of the thesis, we proposed a technique for significant wave height estimation from the received electric field of a radar with the transmitter on a floating platform. While the ocean surface parameter extraction from the received signal usually requires motion compensation and recovery of the Doppler spectrum, the proposed method can be used to estimate the significant wave height without such preliminary data processing. The windowed variance of the upper envelope of the received electric field is used to calculate the significant wave height. Both the first- and second-order scatters are considered in this technique, and the results are compared with the case when only first-order backscatter is employed. By applying the second-order backscatter in addition to the first-order backscatter, the significant wave height can be estimated with a remarkably lower root-mean-square error. However, this method requires a significant wave height calibration step, which can be done by deploying a wave buoy or by using the significant wave height estimated from spectra, which are motion-compensated by the adapted Barrick method. By applying the proposed technique, significant wave height can be estimated with an RMSE of approximately 11 cm.

The main contribution of this thesis is the development of time-domain methods for ocean surface information extraction from radar data for the case of the antenna system mounted on a floating platform that does not rely on prior knowledge of the motion parameters. Firstly, it is inevitable that errors in measurement and time delays will affect the integrity of motion parameters, as they are obtained by sensors. Hence, developing a method of determining motion parameters from radar signals is

valuable. Secondly, the results of the proposed time-domain techniques illustrate that compensating for the effect of the motion and extracting the significant wave height in the case of an antenna on a floating antenna does not require Doppler spectrum formation.

5.2 Future Work

1. In general, the platform motion will follow a multiple-frequency model. It is worthwhile to check how many frequencies are involved and extend and apply the proposed method in this thesis to more complex models since the methods proposed in this thesis are also applicable to multiple-frequency models.

2. Due to the unavailability of field data, the proposed techniques have been evaluated using synthetic data. It is important to note that real radar experimental data presents additional complexities not accounted for in the models employed in this thesis. Factors such as internal system noise and non-Gaussian external noise can potentially affect the data and the derived results. Therefore, the methods proposed in this thesis may encounter challenges when applied to experimental data. It is crucial to conduct testing on field data collected from a floating platform once such data becomes accessible.

3. The simulations carried out in this thesis focus on the monostatic configuration, where the transmitter is mounted on a floating platform and the receiver remains stationary. This configuration is suitable when shore space is limited and accommodating both the transmitter and receiver is not feasible. However, it is essential to assess the effectiveness of the proposed method in the bistatic case as well.

Bibliography

[1] EDR Shearman. Radio science and oceanography. *Radio science*, 18(3):299–320, 1983.

[2] BJ Lipa, DE Barrick, J Isaacson, and PM Lilleboe. CODAR wave measurements from a North sea semisubmersible. *IEEE Journal of Oceanic Engineering*, 15(2):119–125, 1990.

[3] John Walsh, Weimin Huang, and Eric Gill. The first-order high frequency radar ocean surface cross section for an antenna on a floating platform. *IEEE Transactions on Antennas and Propagation*, 58(9):2994–3003, 2010.

[4] Eric W Gill, Yue Ma, and Weimin Huang. Motion compensation for high-frequency surface wave radar on a floating platform. *IET Radar, Sonar & Navigation*, 12(1):37–45, 2018.

[5] Reza Shahidi and Eric W Gill. Time-domain motion compensation of HF-radar Doppler spectra for an antenna on a moving platform. In *IEEE/OES Twelfth Current, Waves and Turbulence Measurement (CWTM)*, pages 1–4. IEEE, 2019.

[6] John Walsh, Weimin Huang, and Eric Gill. The second-order high frequency radar ocean surface cross section for an antenna on a floating platform. *IEEE transactions on antennas and propagation*, 60(10):4804–4813, 2012.

[7] Yue Ma, Eric W Gill, and Weimin Huang. First-order bistatic high-frequency radar ocean surface cross-section for an antenna on a floating platform. *IET Radar, Sonar & Navigation*, 10(6):1136–1144, 2016.

[8] Yue Ma, Eric W Gill, and Weimin Huang. Bistatic high-frequency radar ocean surface cross section incorporating a dual-frequency platform motion model. *IEEE Journal of Oceanic Engineering*, 43(1):205–210, 2017.

[9] Yue Ma. *Bistatic high frequency radar ocean surface cross section for an antenna on a floating platform*. PhD thesis, Memorial University of Newfoundland, 2017.

[10] Yue Ma, Eric W Gill, and Weimin Huang. High frequency radar cross sections of the ocean surface incorporating pitch and roll motions of a floating platform.

In *2018 OCEANS-MTS/IEEE Kobe Techno-Oceans (OTO)*, pages 1–4. IEEE, 2018.

[11] Guowei Yao, Junhao Xie, Zhenyuan Ji, and Minglei Sun. The first-order ocean surface cross section for shipborne HFSWR with rotation motion. In *2017 IEEE Radar Conference (RadarConf)*, pages 0447–0450. IEEE, 2017.

[12] Guowei Yao, Junhao Xie, and Weimin Huang. First-order ocean surface cross-section for shipborne HFSWR incorporating a horizontal oscillation motion model. *IET Radar, Sonar & Navigation*, 12(9):973–978, 2018.

[13] Guowei Yao, Junhao Xie, and Weimin Huang. HF radar ocean surface cross section for the case of floating platform incorporating a six-DOF oscillation motion model. *IEEE Journal of Oceanic Engineering*, 46(1):156–171, 2020.

[14] Guowei Yao, Junhao Xie, and Weimin Huang. Ocean surface cross section for bistatic HF radar incorporating a six DOF oscillation motion model. *Remote Sensing*, 11(23):2738, 2019.

[15] J Wang, R Dizaji, and AM Ponsford. An analysis of phase array radar system on a moving platform. In *IEEE International Radar Conference*, pages 316–320. IEEE, 2005.

[16] Anthony Bourges, R Guinvarc'h, B Uguen, and R Gillard. Swell compensation for high frequency antenna array on buoys. In *IEEE Antennas and Propagation Society International Symposium*, pages 4789–4792. IEEE, 2006.

[17] Sergei Alexander Schelkunoff. A mathematical theory of linear arrays. *The Bell System Technical Journal*, 22(1):80–107, 1943.

[18] Anthony Bourges, R Guinvarc'h, B Uguen, and R Gillard. High-frequency surface wave radar based on a sea floating antenna concept. *IET microwaves, antennas & propagation*, 3(8):1237–1244, 2009.

[19] Jun-hao Xie, Ye-shu Yuan, and Yong-tan Liu. Experimental analysis of sea clutter in shipborne HFSWR. *IEE Proceedings-Radar, Sonar and Navigation*, 148(2):67–71, 2001.

[20] Chunlei Yi, Zhenyuan Ji, Junhao Xie, Minglei Sun, and Yang Li. Sea clutter suppression method for shipborne high-frequency surface-wave radar. *IET Radar, Sonar & Navigation*, 10(1):107–113, 2016.

[21] Di Zhu, Jiong Niu, Ming Li, Ling Zhang, Yonggang Ji, and QM Jonathan Wu. Motion parameter identification and motion compensation for shipborne HF-SWR by using the reference RF signal generated at the shore. *Remote Sensing*, 12(17):2807, 2020.

[22] Maorong Chen, Jiong Niu, Ming Li, Ling Zhang, Yonggang Ji, Wenxiang Wan, and QM Jonathan Wu. A motion compensation method for shipborne HFSWR by using dual reference RF signals generated onshore. *Remote Sensing*, 14(5):1055, 2022.

[23] Sepideh Hashemi, Reza Shahidi, and Eric W. Gill. Platform motion parameter estimation from synthetic high-frequency radar data. *30th Annual Newfoundland Electrical and Computer Engineering Conference*, pages 1–4, 2021.

[24] The MathWorks Inc. Matlab version: 9.10.0 (R2021a), 2020.

[25] Yonggang Ji, Yiming Wang, Weimin Huang, Weifeng Sun, Jie Zhang, Ming Li, and Xiaoyu Cheng. Vessel target echo characteristics and motion compensation for shipborne HFSWR under non-uniform linear motion. *Remote Sensing*, 13(14):2826, 2021.

[26] Klaus Hasselmann. Determination of ocean wave spectra from Doppler radio return from the sea surface. *Nature Physical Science*, 229(1):16–17, 1971.

[27] Donald E Barrick. Extraction of wave parameters from measured HF radar sea-echo Doppler spectra. *Radio Science*, 12(3):415–424, 1977.

[28] Randy Howell and John Walsh. Measurement of ocean wave spectra using narrow-beam he radar. *IEEE Journal of Oceanic Engineering*, 18(3):296–305, 1993.

[29] SF Heron and ML Heron. A comparison of algorithms for extracting significant wave height from HF radar ocean backscatter spectra. *Journal of Atmospheric and oceanic technology*, 15(5):1157–1163, 1998.

[30] Hao Zhou and Biyang Wen. Wave height extraction from the first-order Bragg peaks in high-frequency radars. *IEEE Geoscience and Remote Sensing Letters*, 12(11):2296–2300, 2015.

[31] Yingwei Tian, Zhen Tian, Jiurui Zhao, Biyang Wen, and Weimin Huang. Wave height field extraction from first-order Doppler spectra of a dual-frequency wide-beam high-frequency surface wave radar. *IEEE Transactions on Geoscience and Remote Sensing*, 58(2):1017–1029, 2019.

[32] Zhen Tian, Yingwei Tian, Biyang Wen, Sijie Wang, Jiurui Zhao, Weimin Huang, and Eric W Gill. Wave-height mapping from second-order harmonic peaks of wide-beam HF radar backscatter spectra. *IEEE Transactions on Geoscience and Remote Sensing*, 58(2):925–937, 2019.

[33] Reza Shahidi and Eric W Gill. A new automatic nonlinear optimization-based method for directional ocean wave spectrum extraction from monostatic HF-radar data. *IEEE Journal of Oceanic Engineering*, 46(3):900–918, 2020.

[34] Chen Zhao, Min Deng, Zezong Chen, Fan Ding, and Weimin Huang. Ocean wave parameters and nondirectional spectrum measurements using multifrequency HF radar. *IEEE Transactions on Geoscience and Remote Sensing*, 60:1–13, 2021.

[35] Min Deng, Chen Zhao, Zezong Chen, Fan Ding, and Ting Wang. Wave height and wave period measurements using small-aperture HF radar. *IEEE Transactions on Geoscience and Remote Sensing*, 60:1–12, 2022.

[36] Rachael L Hardman and Lucy R Wyatt. Inversion of HF radar Doppler spectra using a neural network. *Journal of Marine Science and Engineering*, 7(8):255, 2019.

[37] Reza Shahidi and Eric W Gill. Two new methods for the extraction of significant wave heights from received HF-radar time series. *IEEE Geoscience and Remote Sensing Letters*, 17(12):2070–2074, 2020.

[38] Reza Shahidi and Eric W Gill. Extraction of significant wave heights from received HF-radar time series. *IEEE JOE*, 17(12):2070–2074, 2023.

[39] Lei Zhang, Haining Lu, Jianmin Yang, Tao Peng, and Longfei Xiao. Low-frequency drift forces and horizontal motions of a moored FPSO in bi-directional swell and wind-sea offshore west Africa. *Ships and Offshore Structures*, 8(5):425–440, 2013.

[40] Randy Keith Howell. An algorithm for the extraction of ocean wave spectra from narrow beam HF radar backscatteer. Master's thesis, Memorial University of Newfoundland, 1990.

[41] Eric William Gill. The scattering of high frequency electromagnetic radiation from the ocean surface: An analysis based on a bistatic ground wave radar configuration. PhD thesis, Memorial University of Newfoundland, 1999.

[42] Satish Kumar Srivastava. Scattering of high-frequency electromagnetic waves from an ocean surface: an alternative approach incorporating a dipole source. PhD thesis, Memorial University of Newfoundland, 1984.

[43] Donald E Barrick. Theory of HF and VHF propagation across the rough sea, 1, the effective surface impedance for a slightly rough highly conducting medium at grazing incidence. *Radio Science*, 6(5):517–526, 1971.

[44] Willard J Pierson Jr and Lionel Moskowitz. A proposed spectral form for fully developed wind seas based on the similarity theory of SA Kitaigorodskii. *Journal of geophysical research*, 69(24):5181–5190, 1964.

[45] Michael S Longuet-Higgins. Observations of the directional spectrum of sea waves using the motions of a floating buoy. *Ocean wave spectra*, 1961.

[46] Willard J Pierson Jr. Wind generated gravity waves. In *Advances in geophysics*, volume 2, pages 93–178. Elsevier, 1955.

[47] Eric W Gill and John Walsh. A combined sea clutter and noise model appropriate to the operation of high-frequency pulsed Doppler radar in regions constrained by external noise. *Radio Science*, 43(04):1–15, 2008.

[48] Milton Abramowitz, Irene A Stegun, and Robert H Romer. Handbook of mathematical functions with formulas, graphs, and mathematical tables, 1988.

[49] Erik Byholt Hanssen. Coupled analysis of a moored sevan hull by the use of OrcaFlex. Master's thesis, Institutt for marin teknikk, 2013.

[50] Hongjian Cao, Xuyang Wang, Yuanchuan Liu, and Decheng Wan. Numerical prediction of wave loading on a floating platform coupled with a mooring system. *The Twenty-third International Offshore and Polar Engineering Conference*, 2013.

[51] J Walsh and EW Gill. An analysis of the scattering of high-frequency electromagnetic radiation from rough surfaces with application to pulse radar operating in backscatter mode. *Radio Science*, 35(6):1337–1359, 2000.

[52] Michael Selwyn Longuet-Higgins. The statistical analysis of a random, moving surface. *Philosophical Transactions of the Royal Society of London. Series A, Mathematical and Physical Sciences*, 249(966):321–387, 1957.

[53] Kim E Mittendorf. Joint description methods of wind and waves for the design of offshore wind turbines. *Marine Technology Society Journal*, 43(3), 2009.

[54] Sepideh Hashemi, Reza Shahidi, and Eric W Gill. Blind time-domain motion compensation for synthetic Doppler spectra obtained from an HF-radar on a floating platform. *IET Radar, Sonar & Navigation*, 2022.